

**AN EXPERIMENTAL INVESTIGATION OF THE  
POINTED FOREBODY AERODYNAMICS**

**By**

**CAPTAIN ALAN CHARLES STEWART**

**B.Eng., The Royal Military College of Canada, 1981**

**A THESIS SUBMITTED IN PARTIAL FULFILLMENT OF THE REQUIREMENTS  
FOR THE DEGREE OF  
MASTERS OF APPLIED SCIENCE**

**in**

**THE FACULTY OF GRADUATE STUDIES**

**(Department of Mechanical Engineering)**

**We accept this thesis as conforming  
to the required standard**

**THE UNIVERSITY OF BRITISH COLUMBIA**

**August 1988**

**© Copyright Alan Charles Stewart, 1988**

In presenting this thesis in partial fulfilment of the requirements for an advanced degree at the University of British Columbia, I agree that the Library shall make it freely available for reference and study. I further agree that permission for extensive copying of this thesis for scholarly purposes may be granted by the head of my department or by his or her representatives. It is understood that copying or publication of this thesis for financial gain shall not be allowed without my written permission.

Department of Mechanical Engineering

The University of British Columbia  
Vancouver, Canada

Date 2 August, 1988

**ABSTRACT**

An experimental investigation into the pointed forebody aerodynamics has been conducted with particular emphasis on the high angle of attack, zero yaw, side force experienced by fighter aircraft and missiles. Towards this end, a slender cone-cylinder model was tested in the low speed wind tunnel with various passive and active side force alleviation devices installed. The asymmetric flow field, induced by the tip generated pair of helical vortices, and its effects on the model are investigated in the presence of several cone tip geometries: a family of nose-booms; a set of delta strakes; a porous tip; spinning nose-boom tips; as well as the standard cone tip. The effectiveness of each tip in reducing the side force is assessed over a range of flight conditions, and compared with the corresponding standard tip data. Reductions in the side force of up to 50% with nose-booms; 88% with delta strake tips; 50% with a porous tip; and up to 75% with spinning nose-booms have been achieved. The applicability and practicality of these devices in aircraft applications are also considered, however, only in a preliminary fashion.

## TABLE OF CONTENTS

1	INTRODUCTION. . . . .	1
1.1	Preliminary Remarks. . . . .	1
1.2	A Brief Review of the Relevant Literature . . . . .	4
1.3	Purpose and Scope of the Investigation. . . . .	13
2	MODELS AND TEST PROCEDURES . . . . .	15
2.1	Cone Model . . . . .	15
2.2	Tip Geometries. . . . .	17
2.3	Wind Tunnel. . . . .	21
2.4	Instrumentation. . . . .	23
2.5	Test Procedures. . . . .	25
3	RESULTS & DISCUSSIONS. . . . .	28
3.1	Standard Cone Tip Roll Tests. . . . .	28
3.2	Nose-Boom Tests. . . . .	37
3.3	Delta Strake Tests. . . . .	43
3.4	Porous Tip Tests. . . . .	52
3.5	Spinning Tip Tests. . . . .	56
4	CONCLUDING REMARKS. . . . .	65
4.1	Conclusions. . . . .	65
4.2	Recommendations. . . . .	69
	BIBLIOGRAPHY. . . . .	73
	APPENDIX I: INTEGRATION OF PRESSURE DATA. . . . .	78

## LIST OF FIGURES

Figure 1-1	Effect of angle of attack on the lee-side flow field . . . . .	2
Figure 2-1	The standard cone mounted in the wind tunnel at an angle of attack of $30^\circ$ . . . . .	16
Figure 2-2	An exploded view of the cone-model. . . . .	16
Figure 2-3	A section view of the cone model . . . . .	18
Figure 2-4	The brass apex cone tip containing 16 pressure taps. . . . .	19
Figure 2-5	The porous cone tip . . . . .	19
Figure 2-6	The bearing housing cone segment. . . . .	20
Figure 2-7	A family of nose-boom tips with the standard tip shown for comparison. . . . .	20
Figure 2-8	A family of delta strake tips used in the test program. . . . .	22
Figure 2-9	A schematic diagram of the low speed wind tunnel used in the experiments. . . . .	22
Figure 2-10	The scanivalve pressure line switching arrangement. . . . .	24
Figure 2-11	The Barocel pressure transducer and electronic manometer. . . . .	24
Figure 2-12	Instrumentation layout for pressure measurements using a Scanivalve and a Barocel transducer. . . . .	25
Figure 3-1	Pressure distribution at a reference station P, as affected by the angle of attack, for the standard tip at zero roll angle. . . . .	30
Figure 3-2	Pressure distribution at a reference station P, as affected by the angle of attack, for the standard tip at a roll angle of $300^\circ$ . . . . .	31
Figure 3-3	Variation of the side force coefficient for the standard tip model with pitch and roll. . . . .	32

Figure 3-4	Variation of the normal force coefficient for the standard tip model with pitch and roll. . . . .	33
Figure 3-5	Effect of the standard tip roll position on the side force at a pitch angle of $50^\circ$ . . . . .	35
Figure 3-6	Effect of the standard tip roll position on the normal force. . . . .	36
Figure 3-7	Effect of boom length on variation in the side force coefficient with pitch and roll attitudes:	
	a) $L_b = 4.13$ cm, $L_b/L = 0.27$ ;	
	b) $L_b = 3.18$ cm, $L_b/L = 0.21$ ;	
	c) $L_b = 2.54$ cm, $L_b/L = 0.17$ . . . . .	38
	d) $L_b = 1.91$ cm, $L_b/L = 0.125$ ;	
	e) $L_b = 1.27$ cm, $L_b/L = 0.083$ ;	
	f) $L_b = 0.95$ cm, $L_b/L = 0.063$ . . . . .	40
	g) $L_b = 0.64$ cm, $L_b/L = 0.042$ ;	
	h) $L_b = 0.32$ cm, $L_b/L = 0.031$ ;	
	i) $L_b = 0.16$ cm, $L_b/L = 0.010$ . . . . .	41
Figure 3-8	Magnitude of the maximum side force coefficient with varying nose-boom length including the standard tip case. . . . .	42
Figure 3-9	Normal force variation with pitch angle and roll orientation for the 4.13 cm nose-boom. . . . .	44
Figure 3-10	Normal force coefficient variation with pitch incidence and nose-boom length. . . . .	45
Figure 3-11	Variation of the side force coefficient with pitch and roll angles for the 3.18 cm delta strake. . . . .	46
Figure 3-12	Pressure distribution, at the reference station P, for the standard tip at a yaw incidence of:	
	a) $\beta = -10^\circ$ . . . . .	48
	b) $\beta = +10^\circ$ . . . . .	49
Figure 3-13	Variation of the side force coefficient with pitch and yaw angles as affected by the delta strake length (aspect ratio = 1):	
	a) standard tip, $L_s/L = 0$ ;	
	b) $L_s = 0.32$ cm, $L_s/L = 0.021$ ;	
	c) $L_s = 0.64$ cm, $L_s/L = 0.042$ . . . . .	50
	d) $L_s = 1.27$ cm, $L_s/L = 0.083$ ;	
	e) $L_s = 1.91$ cm, $L_s/L = 0.125$ ;	
	f) $L_s = 2.54$ cm, $L_s/L = 0.167$ ;	
	g) $L_s = 3.18$ cm, $L_s/L = 0.208$ . . . . .	51

Figure 3-14	Effect of the strake length on the magnitude of the side force. . . . .	53
Figure 3-15	Variation of the normal force coefficient with pitch and yaw angles for a strake of 3.18 cm. . . .	54
Figure 3-16	Effect of the strake length on the normal force coefficient. . . . .	55
Figure 3-17	Side force variation as affected by the pitch angle and nose-boom length at tip spin of 2000 rpm . . . . .	57
Figure 3-18	Effect of the nose-boom length on the side force coefficient at 2000 rpm. . . . .	59
Figure 3-19	Side force variation as affected by the pitch angle and spin rate for a 1.27 cm nose-boom . . . . .	.60
Figure 3-20	Effect of spin rate on the side force coefficient for a 1.27 cm nose-boom . . . . .	.61
Figure 3-21	The normal force coefficient as affected by: a) the nose-boom length at a spin rate of 2000 rpm. . . . . b) the spin rate for a 1.27 cm nose-boom. . . . .	.63 .64
Figure I-1	Division of the cone surface into area segments. . . . .	.78

## LIST OF SYMBOLS

$A_b$	base area of cone, $\pi D^2/4$
$a$	local speed of sound
$C$	perimeter of a regular polygon of $n$ sides
$C_N$	coefficient of normal force, normal force/ $(q \cdot A_b)$
$C_P$	coefficient of pressure, $P/q$
$C_S$	coefficient of side force, Side Force/ $(qA_b)$
$D$	cone base diameter
$L$	total cone length
$L_b$	nose-boom length
$L_i$	length of the cone to the station $i$
$L_s$	strake length
$M$	Mach number, $V/a$
$n$	an integer, number of sides of a polygon
$P, P_\infty$	local and reference free stream static pressures, respectively
$q$	free stream dynamic pressure head, $(1/2)\rho V_\infty^2$
$Re$	Reynolds number, $VD/\mu$
$R_i$	radius of the cone at the station $i$
$S_i$	length of the side of a regular polygon
$V, V_\infty$	local and free stream velocities, respectively
$\alpha$	angle of attack
$\beta$	yaw angle
$\delta$	cone half-angle

$\rho$	density
$\phi$	roll angle (in the circumferential direction) to reference point on the surface of the cone
$\theta$	angular position in roll w.r.t. a fixed reference frame
$\theta_i$	circumferential position on the cone surface at the point $i$
$\mu$	viscosity

## ACKNOWLEDGEMENTS

The timely completion of this thesis would not have been possible without the assistance of many individuals and organizations. First and foremost gratitude is expressed for the guidance and counsel of Dr. V.J. Modi. His clear insight into the technical part of the thesis and his invaluable editorial skills are greatly appreciated.

The comraderie and occasional brainstorming sessions with my fellow graduate students have made my entire masters program including the thesis, both more enjoyable and progress faster.

The machine and instrumentation shop technicians have helped me with their expertise when needed. Their assistance has been invaluable. In particular, Len Drakes contributed his exceptional model making skills.

The Canadian Armed Forces completely covered all financial costs of this post-graduate education and to them I am grateful for both the financial assistance and the opportunity. Many local agencies of the Canadian Armed Forces have been particularly helpful over the last years. Sargent Daniels of Jericho Detachment and the Photo Section of Canadian Forces Base Chilliwack deserve special mention.

## 1 INTRODUCTION

### 1.1 Preliminary Remarks

It is well known that certain flight vehicles, particularly the STOL and fighter airplanes, often undertake maneuvers at relatively high angles of attack. It has been observed that, depending upon the geometry of the aircraft and its angle of attack, it may experience a large side force, of uncertain direction, resulting in a yawing moment that may prove difficult to control. Association of a side force with an object that has a plane of symmetry intrigued aerodynamicists, however, it was quickly established to be related to the fluid mechanics of pointed forebodies. In the case of an aircraft, it would be the nose of the fuselage. Tip-tanks, bombs, missiles, launch vehicles, hubs of propellers, etc., also present pointed forebody geometries. Normally, such a pointed forebody is incorporated as a part of the streamlined structure to reduce drag, increase stability and aid in generating lift. Although a simple cone geometry is sometimes used, a more common pointed forebody is a tangent ogive or its variation.

As discussed by Ericsson and Reding [1], an object with a slender forebody, depending upon its attitude in pitch, exhibits four distinctly different types of flow patterns as shown in Figure 1-1.

At low angles of attack the flow field is usually symmetric and essentially attached. As the pitch angle increases the streamlines are swept downstream from the windward to the leeward side of the body symmetrically about the pitch plane.

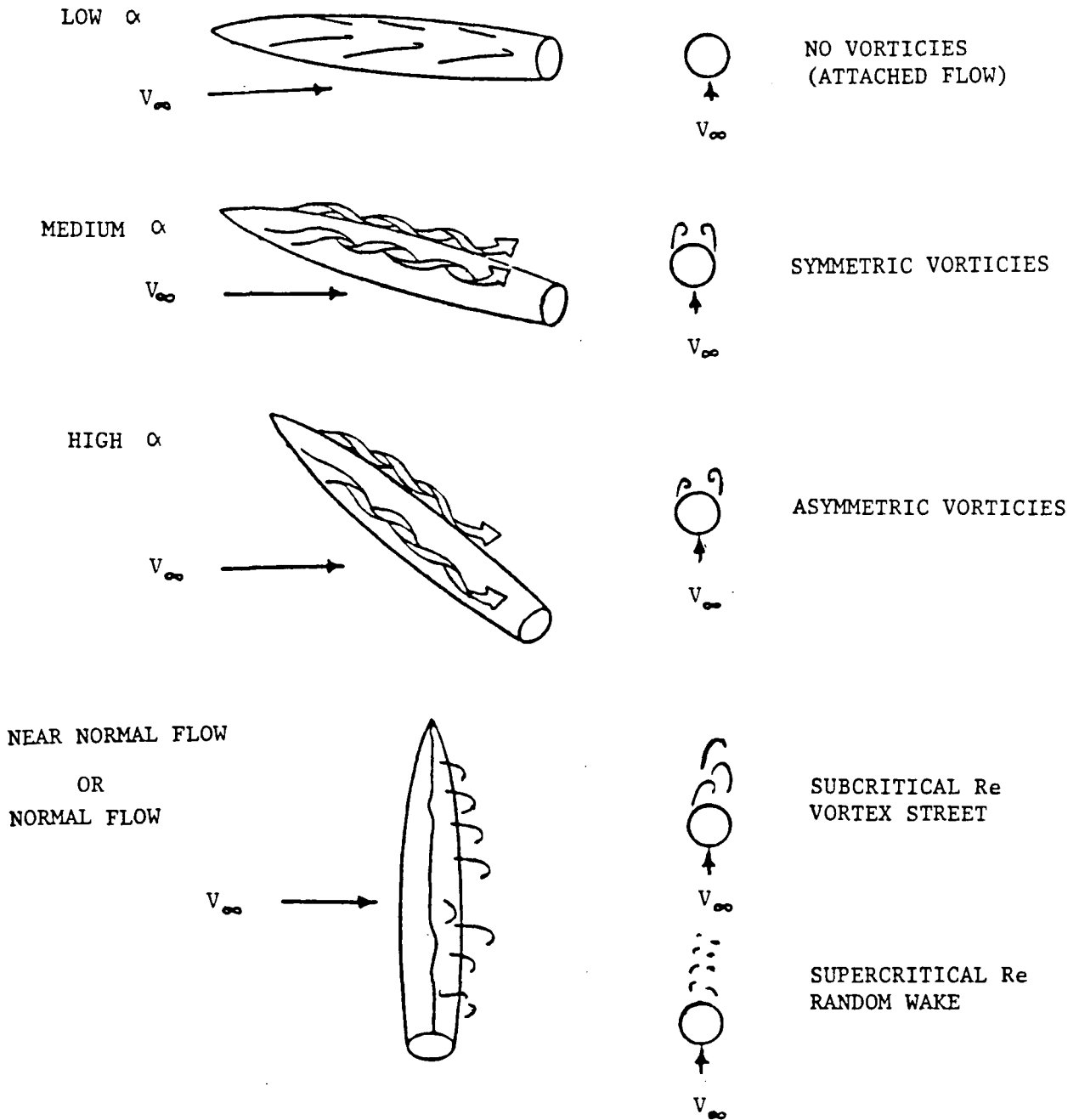


Figure 1-1. Effect of angle of attack on the lee-side flow field.

At higher angles of attack the flow becomes separated. Typically, two counterrotating, symmetric, stationary vortices form on the leeward side of the object, starting at or near the apex and continuing well downstream of the object.

At still higher angles of attack the vortices become asymmetric. One vortex of the pair changes strength and position such that it exerts a lower aerodynamic pressure on the body than the other. This results in a net side force which is the subject of study in this thesis. Although this flow pattern has been described and analyzed in the literature in terms of two vortices, effectively there can be four, six or more stationary quasisteady vortices.

At angles of attack approaching flow normal to the slender body the stationary vortices start to shed. A vortex street or a more random wake results and the side force becomes oscillatory or disappears entirely.

The onset of a significant side force usually occurs at an angle of attack approximately twice the cone half-angle, and at its peak can be of the same order of magnitude as the lift generated by the forebody. On aircraft this would correspond to an angle of attack when the rudder is partially shadowed by the wake of the fuselage. This may lead to the situation where the side force is an order of magnitude larger than the correcting force available from the rudder.

As the onset of the side force is usually at a fairly high angle of attack, it is not a problem for most aircraft. Only highly maneuverable craft capable of flights at large angles of attack have experienced the side force phenomena. Included within this group are the latest

fighters, the F-16, F-18, etc., together with air-to-air and surface-to-air missiles. For reasons of nose shape, flight attitude and the Mach number the Space Shuttle largely avoids the side force phenomena.

The effectiveness of tip geometry in partial alleviation of the side forces experienced by pointed forebodies is the topic of investigation here. The flow field is fully three-dimensional, unsteady, vortex dominated, and primarily governed by the boundary layer. It also exhibits puzzling, seemingly random characteristics thus making this problem of contemporary interest and significance, rather challenging.

## 1.2 A Brief Review of the Relevant Literature

The side force phenomenon was first noticed and documented by Allen and Perkins [2] in 1951. Since then many researchers have experimented with various aspects of the problem. Most of the early investigations [2-4] concentrated on flow past slender cylinders with various nose geometries. They focused their study on the flow field aft of the nose. Only more recently [5-13] has the focus moved to the forebody nose itself.

A review of the literature suggests that the early research efforts can be broadly divided into two groups. On one hand, we have investigators who consider the side force phenomenon to be boundary layer governed and treat it as a logical extension of the two-dimensional cylinder flow. The Reynolds number dependence and the effectiveness of some of the side force alleviation devices seem to support this view. Other researchers suggest that the side force is caused by a basic hydrodynamic instability of the leeward flow. Some experimental results,

such as the direction switching of the side force and effects of normal blowing, substantiate this concept.

It appears that these two hypotheses are not mutually exclusive. A hydrodynamic instability of the leeward flow could be quite sensitive to an asymmetric boundary layer upstream. Conversely, the high pressure gradients in the streamwise direction may make the boundary layer separation sensitive to the external flow.

Thompson and Morrison [3] studied the spacing, position and strength of vortices behind slender cylinders. They used schlieren photography and yawmeter traverses to investigate the flow field in the wake of a cone-cylinder model. Their concern was mostly in the drag and vortex shedding from the cylindrical body, and they have presented useful data on the subject up to a Mach Number of one.

Lamont and Hunt [4] tested a slender cylinder in laminar flow with four different nose geometries. Their pressure tapped cylinder could be fitted with a 2, 4, or 6 calibre ogive nose or a nose-cone of  $L/D = 2$ . The results demonstrated a clear dependence on the Reynolds number, however, they were plagued by a lack of repeatability. It was postulated that the flow was unsteady as it exhibited clear evidence of switching of pattern between two configurations. A change in the roll angle was used to further demonstrate the unsteadiness.

Rao [5] suggested that a properly designed boundary layer trip could stabilize the side force by disrupting the vortex feeding mechanism. He installed a pair of symmetrical helical trips on the nose of an F-5 aircraft model and tested its static and dynamic response at high angles of attack. His results showed better response in all flight

conditions except sideslip where the trips decreased the directional stability. The trips, however, did not disrupt the vortex feeding mechanism but did keep the separated vortices symmetrical throughout a much larger flight envelope.

Oberkampf and Bartel [14] studied the wake of an ogive nosed cylinder in a supersonic flow. Although they demonstrated some interesting characteristics of the wake, the investigation was confined to symmetric flows at relatively low incidence.

Ericsson and Reding have contributed rather extensively to the field. Their best known papers [1,6,7,15] are reviews of the existing literature, and critical analysis of the results with conclusions based upon both the previous work and their own. In particular, reference [6] focuses on the vortices created by the nose and methods of alleviating the side force. It suggests the usefulness of nose bluntness, nose-boom, and various geometries of boundary layer trips, in reducing the side force and presents results showing the effectiveness of the trips with an F-111 aircraft model. They concluded that nose bluntness and nose-boom can alleviate the side force to various degrees. On the other hand, trips and strakes, although more effective, have a disadvantage for an aircraft not flying coordinated maneuvers.

Further evidence of the leeside flow instability hypothesis was presented by Oberkampf, Owen and Shivananda [16] in their investigation of high subsonic flow past a pointed slender body. They used a Laser Doppler Velocimeter (LDV), force and moment measurements, surface hot wires and laser vapour screen photography in their experiments. The results clearly showed that more than one asymmetric

vortex wake configuration can exist for the same angle of attack and roll angle.

Another paper by Ericsson and Reding [15] concentrated on moving wall effects. The influence of spin, coning and pitch rate on the side force phenomenon were analyzed. The effects of varying the Reynolds and Mach numbers on the side force were also discussed. A clear dependence of the direction of the side force on the body motion was demonstrated particularly within a critical Reynolds number range. The study showed a positive coupling between the coning motion and the vortex shedding such that the pressure distribution increased the coning rate.

Peake, Owen and Johnson [8] conducted studies with an LDV, the Laser Vapour Screen Visualization, pressure measurements and buried wire instruments on a  $5^\circ$  cone and a  $16^\circ$  tangent ogive. Besides conjecturing upon the mechanisms triggering the initial asymmetry, they also proposed a novel means of controlling the orientation of the side force utilizing a small amount of blowing quite close to the nose. It was demonstrated that blowing on one side of the nose could reverse the side force, and that the normal blowing works better than either the upstream or the downstream tangential blowing.

Skow, Moore and Lorincz [9] carried the concept of active blowing a step further. They completed a combined experimental and analytical study to control asymmetric vortex formation from an aircraft forebody with the aim of developing an automatic spin recovery system. From the results of the wind tunnel tests with tangential blowing a six degree of freedom digital simulation of aircraft performance was developed to show

that the concept could substantially improve the spin recovery of fighters. They also showed that a small amount of blowing at high angles of attack can produce more yawing moment than that obtained through the rudder.

Erickson and Lorincz [10] studied the effects of helical trips on a model of a fighter aircraft, the F-5. Their water tunnel and wind tunnel tests concluded that properly designed helical trips significantly reduced the asymmetric loads at zero sideslip, however, a large decrease in lateral-directional stability was also noted.

Yanta and Wardlaw [17] conducted some fundamental research on the flowfield structures associated with slender bodies. It was found that the maximum local side force occurs as the first vortex is shed, and is towards the side of the remaining vortex. Unfortunately the results were plagued with the repeatability problems, also faced by many other researchers, hence their observations can only be considered qualitative in nature.

Almosnino and Rom [18] experimented with symmetrical blowing and circular trips on a slender body. They found both the devices effective in reducing the side force but the blowing rate required to significantly alleviate the side force became very large at transonic and supersonic speeds. It was concluded that symmetrical blowing is a simple and easy procedure to implement in existing and future aircraft.

Peake, Fisher and McRae [19] studied separated flow behind a 5° cone at Mach numbers of 0.6, 1.5 and 1.8 in flight, as well as through wind tunnel and numerical experiments. They found a reasonable

agreement between the three sets of results, however, the experiments avoided test angles of attack which might produce an asymmetric flow.

Lamont [20] contributed an article which has proven very important to the understanding of the side force phenomenon. He conducted wind tunnel tests with an extensively instrumented ogive-cylinder in laminar, transition and turbulent separation conditions. The results clearly demonstrated a need to vary roll angle in any series of comprehensive tests. He conjectured that microscopic surface asymmetries at the apex of the body were sufficient to trigger large scale flow asymmetries further downstream.

Keener et al. [21] further substantiated Lamont's thoughts on the cause of the side force onset. His experiments involved measuring the side force while first rolling his entire model and then rolling the tip alone. The results, nearly identical in the two tests, support the microasymmetry hypothesis.

Woolard [22] used a conformal mapping technique to add weight to the hydrodynamic instability argument. Some researchers have postulated that boundary layer effects, associated with asymmetric separation points, cause vortex asymmetry. Others, by comparing the forebody vortices to the slender wing vortices, postulate a hydrodynamic instability resulting from the crowding of vortex lines at the apex despite symmetric separation. Woolard, by successfully comparing cone side force onset angles, through the appropriate mappings, to slender delta wing experimental data, concluded that the separation lines are unimportant in relation to the basic hydrodynamic instability.

Apart from the numerical work of Peak et al. [19] mentioned previously, other avenues of computer modeling of the airflow around slender bodies have also been attempted. Almosnino and Rom [23] using potential flow theory, with a combination of source and vortex-lattice elements to represent the body, successfully modeled real symmetrical flows. Almosnino [24] extended this computer model to asymmetric flows at higher angles of attack. The only input needed for a realistic modeling was the location of the separation lines on the body.

Newsome and Adams [25] have solved the Reynolds-averaged Navier-Stokes equations for flow about an elliptical body missile. Numerical results were obtained for the vortex dominated flow at  $10^\circ$  and  $20^\circ$  angles of attack with  $0^\circ$  and  $45^\circ$  roll. They used a high speed vector-processor computer, the Cyber 205. Excellent agreement was found with their experimental results.

Chan [26] used a far field approach to study the side force on a slender body. He numerically modeled the far field wake by a system of trailing vortex filaments, and established a relationship between the force distribution and the structure of the wake. The geometry and strength of the filaments were derived from experimental data and the dynamics of the system. The procedure appears quite promising as the numerical predictions showed excellent correlation with the experimental results.

In the review article by Reding and Ericsson [7] three hypotheses were proposed which were supported by the new evidence: the maximum side force occurs when a subcritical separation is experienced on one side of a body and a supercritical separation appears on the

other; the body motion can lock in a driving vortex asymmetry to produce a self-induced rotation; and a laminar separation can occur on a cylinder when the pointed nose is experiencing a turbulent flow.

In a paper concentrating on the coupling of body motion and vortex shedding referred to earlier, Ericsson and Reding [1] present some interesting results. Tests with a spinning tip at the critical Reynolds number showed that the direction of the spin determines the direction of the side force. The coning action sheds vortices such that the motion is sustained regardless of the direction of the static side force. Hence it appears that the vehicle motion induces asymmetric vortices which easily overpower any static asymmetry.

Seginer and Ringel [27] explored the Magnus effect at high angles of attack and in the critical Reynolds number range. It was observed that the force reversal can occur when, due to the boundary layer effects, the lift is opposite to the classical Magnus contribution. Their experiments demonstrated a complex interdependence of the spin rate, angle of attack, Reynolds number and lift.

Ericsson [28] explored the flat spin of slender bodies and their recovery. He discusses in depth the types of separation possible, the effect of body motion on separation, its attendant lift and the Magnus effect. In a more recent paper on the subject [29] he shows conclusively that the body motion locks in an asymmetric vortex pattern, which drives the slender body into a flat spin.

Viswanath and Narayan [11] conducted tests with a 20° cone at pitch angles up to 47° and over a wide range of the Reynolds number. The information was confined only to the force balance data.

Modi et al. [12] carried out experiments with a circular cylinder to which a set of conical forebodies can be attached. They explored the effects of surface roughness, helical trips, modified tip geometries and tip rotation. Among the side force alleviation devices tested, the nose-boom and tip rotation proved to be the most promising.

In an unpublished fourth year engineering project report by Bishop, Tarnai, and Thornthwaite [13], tests on a 28° cone in subsonic flow indicate that, among the various nose geometries tried, the delta-strake tip had the most promise in terms of the side force reduction.

Fiddes [30] has presented an excellent summary of several potential flow line vortex and vortex sheet models for flow past an inclined cone. He divides the numerical results into two categories. The first family of solutions require asymmetric separation lines to produce asymmetric flow results. The second family of solutions are capable of producing asymmetric vortex core locations even when fed from symmetric separation positions. His own contribution to the problem was the development of a numerical scheme using vortex sheet methods, some clever formulae and parametric manipulations which produced the second family of results. The numerical results compared quite favourably with the experimental data.

Marconi [31] has also contributed some interesting numerical results, for highly vortical flows past cones and delta wings in the supersonic regime, using an Euler equation model. Two sources of vorticity are studied: the flow field shock system; and the separating boundary layer. Solutions obtained with both the sources of vorticity

are studied in detail, and compared with each other, with the potential flow calculations and the experimental data.

It is apparent from the literature that the problem of side force experienced by high performance aerospace vehicles has received active attention relatively recently. Some progress has been made in understanding of the phenomenon at a fundamental level and there are several hypotheses which seem to explain some aspects of the mechanism of the side force generation. On the other hand, the experimental results are often not reproducible, suggesting that the models used in explaining the phenomenon are, at best, incomplete.

### 1.3 Purpose and Scope of the Investigation

With this as background, the thesis aims at providing more precise information, obtained through a set of carefully planned experiments, assuring repeatable and reliable data, to better understand the side force phenomenon. It aims at studying the asymmetric flow field associated with a slender cone and assessing effectiveness of several tip devices in alleviating the side force. As apparent from the review the flow field is unsteady, boundary layer sensitive, turbulent, vortex dominated and highly configuration dependent. Furthermore, it is somewhat affected by the Reynolds and Mach numbers. Hence, the problem of high angle of attack forebody aerodynamics does not lend itself to the known analytical or numerical procedures. The present investigation, therefore, purely relies on a carefully planned experimental program.

Several investigators in the past [5,6,9,12,13,18] have tried nose-booms, strakes, trips and surface roughness with varying degrees of success as to their effectiveness in reducing the side force. In most cases the tests have been rather preliminary in nature with results mostly qualitative in character.

The present study attempts to lay a firm foundation for this class of problems through a systematic study with several passive devices which appear promising in reducing the side force. The emphasis is purposely on passive devices as they are deemed to be more practical.

Obviously, the applicability of the device in real-life situation would be the ultimate criterion of its success. Although this aspect is of importance, it is not the prime concern here, the focus being on the fundamental information on performance of the side force alleviation devices. It is recognized that as the nose of an aircraft or a missile is frequently used to house a radar, some of the devices which appear promising in alleviating the side force may prove impractical to implement. The radome, which forms the nose of such aircraft, is usually a thin, uniform, nonmetallic composite shell with no moving parts. Of particular importance are its spectral transmission characteristics, which are required to be as uniform as possible, directionally. Hence, from the radar performance considerations, active moving devices appear impractical. Water absorption and its attendant attenuation of microwaves is likely to make a porous tip alleviation device unsuitable as well. On the other hand, devices such as nose-booms and strakes degrade radar performance only marginally and hence have received particular attention in this thesis.

## 2 MODELS AND TEST PROCEDURES

This chapter briefly describes the models used in the wind tunnel experiments, test arrangement, instrumentation and test procedures. The conventional wind tunnel equipment being standard in any aerodynamics laboratory needs no explanation. Most of the wind tunnel test procedures are also well established. Only distinctive models and instruments with specific role are touched upon here.

### 2.1 Cone Model

For the entire experimental program a cylindrical base, 7 cm in diameter and 10 cm long, with a conical forebody formed the basic test model. The hollow aluminum cone with an apex angle of  $\approx 28^\circ$  was 15.25 cm (6 in.) long and had a base diameter of 7.62 cm (3 in.). It accommodated up to 40 pressure taps. The apex of the cone can be separated at two locations to replace it with desired tip geometries. The cylindrical aft body housed a variable speed d.c. motor to rotate the tip at a controlled speed during one phase of the experimental program. The aftbody was also connected to a yoke type vertical support, in turn mounted on the wind tunnel balance platform, such that the angle of attack and yaw inclination can be adjusted as required. The model, though modified and refined, is essentially the same as the one used by Bishop et al. [13]. Figures 2-1 and 2-2 show the test arrangement for the model and its exploded view, respectively.



Figure 2-1 The standard cone mounted in the wind tunnel at an angle of attack of  $30^\circ$ .

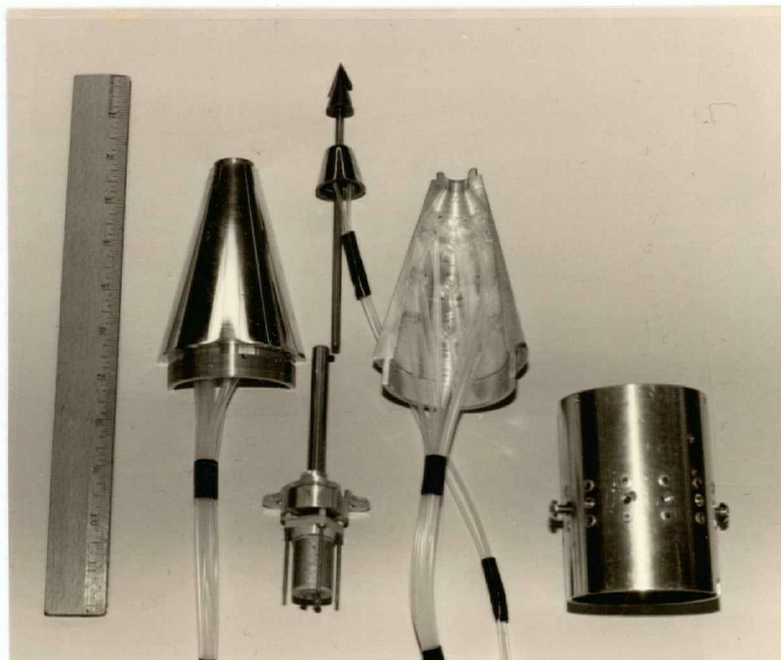


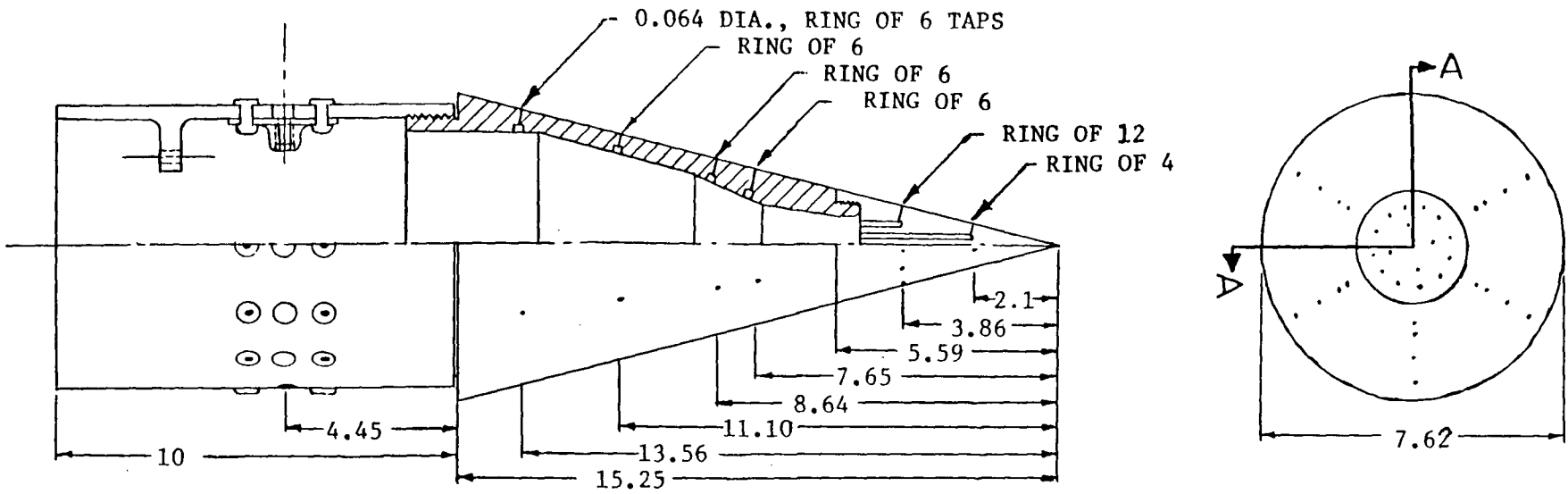
Figure 2-2 An exploded view of the cone-model.

The pressure taps for the standard cone model, i.e. with no tip modification, were equally spaced circumferentially at six stations along its length. In all there were 40 pressure taps distributed on the cone surface as indicated in Figure 2-3. The brass apex of the cone carrying 16 pressure taps (Figure 2-4) can be removed and replaced with a porous tip (Figure 2-5) or a bearing housing (Figure 2-6) provided with three pressure taps. The bearing housing, with the pressure taps, supports different nose-tips, which can now be tested at desired roll orientations, as well as in the spinning mode. The static pressure at a tap, typically 0.64 mm in diameter, is conveyed by a polyethylene tube, 1.7 mm inside diameter, to an externally located pressure transducer.

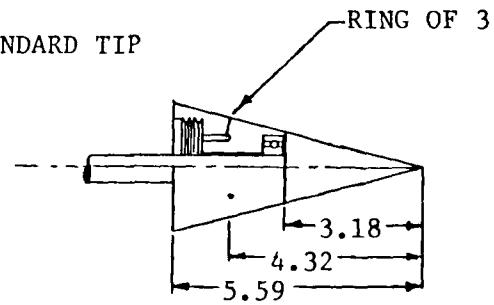
To minimize the effect of the surface roughness on the boundary layer instability, and hence better identify the influence of tip geometry on the side force, the cone model was provided with a smooth mirror finish. With the exception of some of the smaller nose tips, the entire cone was polished to within a 5-7 micron surface roughness. Although the roughness was necessarily higher at junctions of the various components of the cone, the model may be considered essentially smooth.

## 2.2 Tip Geometries

The test program made use of several tip geometries. Besides the standard tip shown in Figure 2-3, a smaller tip (Figure 2-7) was also employed, which can be rotated about its axis quite readily to assess the side force dependence on the roll angle. As discussed in Chapter 1,



SECTION A-A CONE MODEL WITH STANDARD TIP



BEARING HOUSING WITH  
 ROTATABLE STANDARD TIP

Figure 2-3 A section view of the cone model (all dimensions in centimeters).

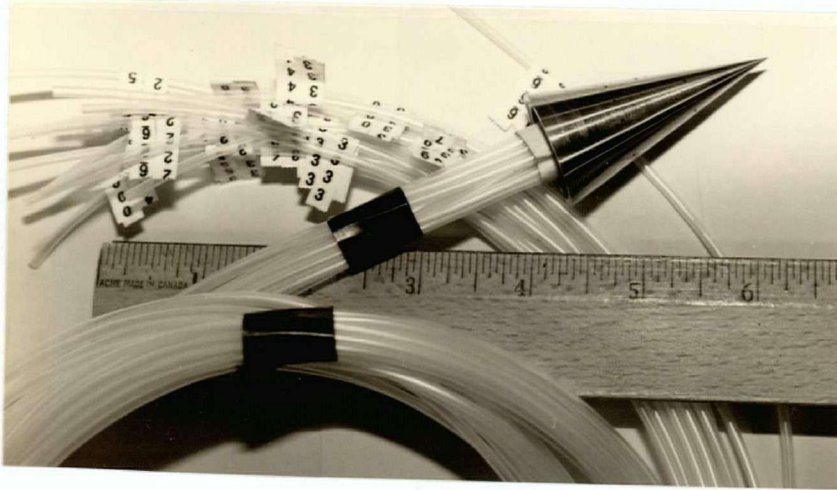


Figure 2-4 The brass apex cone tip containing 16 pressure taps.



Figure 2-5 The porous cone tip.

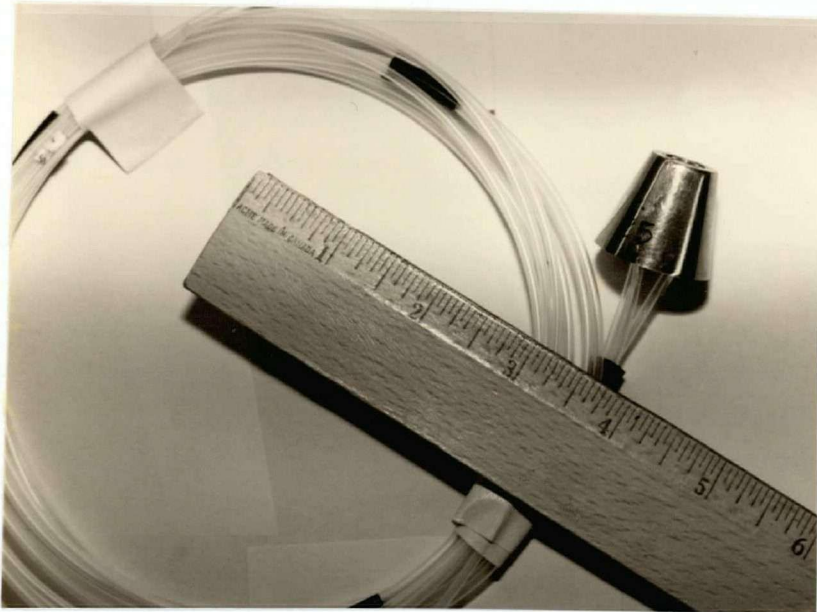


Figure 2-6 The bearing housing cone segment.

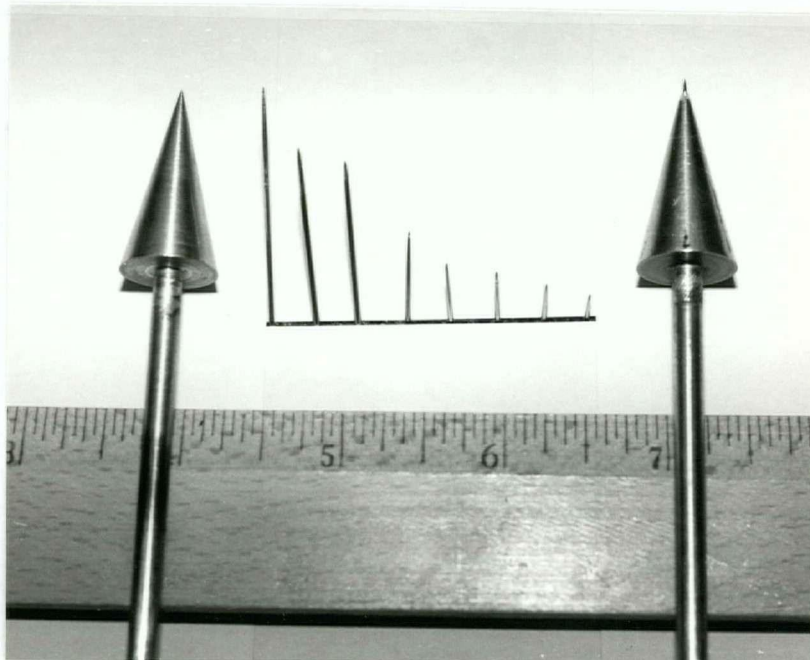


Figure 2-7 A family of nose-boom tips with the standard tip shown for comparison.

Lamont [20] and Keener et al. [21] did observe such roll dependence of the side force.

The tests have focused primarily on two families of tip geometries: nose-boom (Figure 2-7) and delta strake (Figure 2-8). The literature review suggests both the devices to affect the side force [5,6,8,9,12,13]. The nose-boom lengths used in the experiments varied from 2.7 cm to 0.16 cm (aspect ratio variation based on the maximum boom diameter was 46 and 2, respectively). The length of the delta strake varied from 3.2 cm to 0.32 cm with an aspect ratio of 1. As several earlier investigators [5,6,8,9] have observed a loss of lateral-directional stability with the delta-strake, the tests were also conducted at yaw angles of  $\pm 10^\circ$ .

### 2.3 Wind Tunnel

The cone model was tested in a low speed, low turbulence return type wind tunnel where the air speed can be varied from 1 to 46 m/s with a turbulence level less than 0.1%. The pressure differential across the contraction section of 7:1 ratio can be measured on a Betz micromanometer with an accuracy of 0.2 mm of water. The test section velocity is calibrated against the above pressure differential. The rectangular cross-section, 91 cm wide X 69 cm high, is provided with 45° corner fillets which vary from 15 cm X 15 cm to 12 cm X 12 cm to partly compensate for the boundary layer growth. Figure 2-9 shows the tunnel outline.

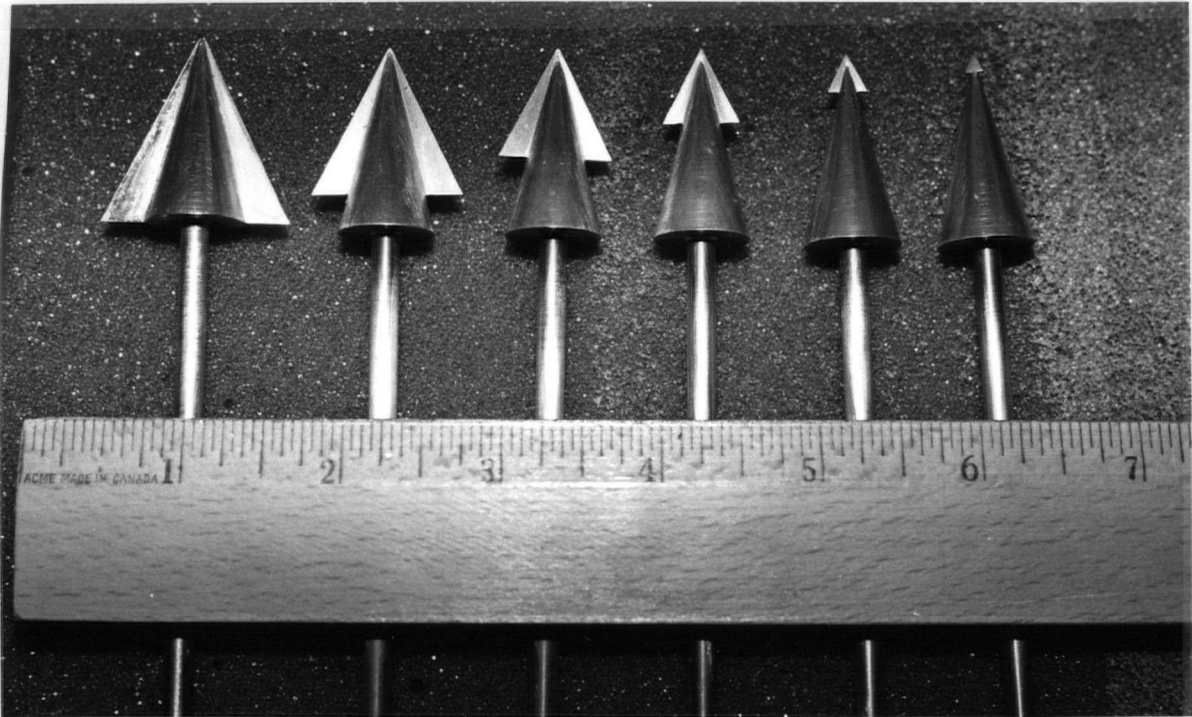


Figure 2-8 A family of delta strike tips used in the test program.

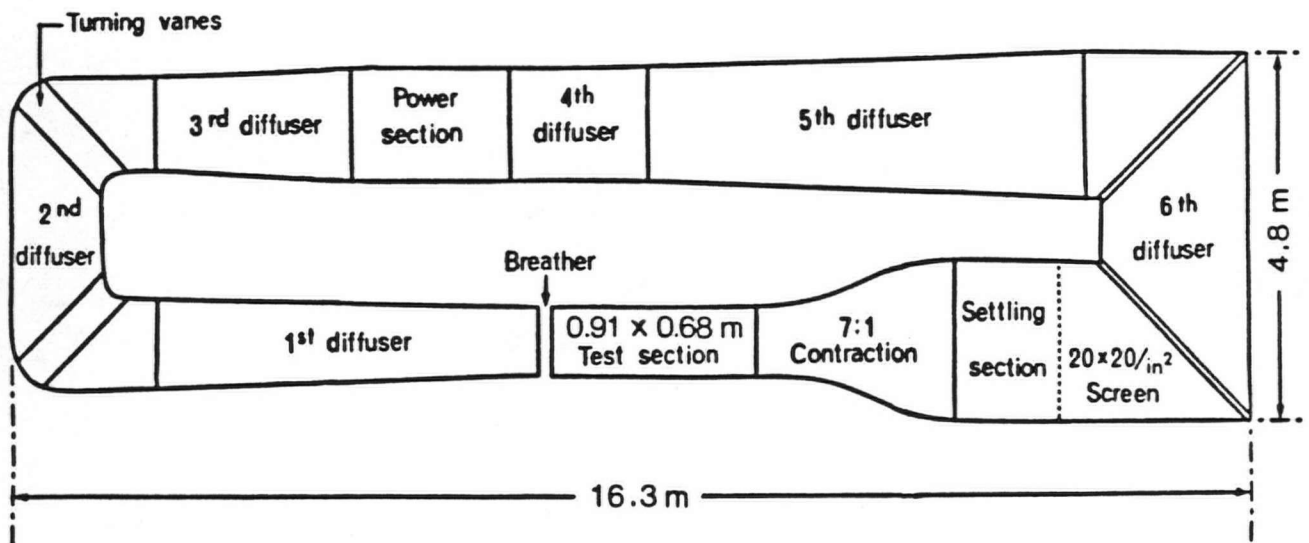


Figure 2-9 A schematic diagram of the low speed wind tunnel used in the experiments.

## 2.4 Instrumentation

Although the primary interest was in the pressure measurements, the model was mounted on a custom built Aerolab supply balance turntable. Besides supporting the model, the turntable can be adjusted to provide any desired angle of attack. The strain gauge balance incorporates an array of six load cells which provide the three orthogonal components of the resultant force (lift, drag and side force), and moment (pitch, roll and yaw) in conjunction with a Leeds and Northrup microvolt amplifier. Due to excessive drift of the instrument, it was used only as a qualitative indicator and hence the balance results are purposely not reported.

The model had 24, 27, or 40 pressure taps depending upon the tip configuration. A scanivalve type 48J9 (Figure 2-10) switching device was used, which connected the pressure taps sequentially to a Datametrics Barocel Pressure Sensor, type 511J-10. The Barocel is a high precision, stable, capacitive voltage divider which measures a differential pressure up to  $\pm 10$  mmHg. The resulting voltage was transmitted to a Datametrics Electronic Manometer, type 1018B (Figure 2-11). The accuracy of the combined Barocel and Electric Manometer system is 0.001 mmHg and the system was found to be in calibration with the Betz Manometer. As the free stream fluctuations were relatively insignificant and for reasons of convenience, the Barocel readings were rounded off to the nearest 0.01 mmHg. A schematic diagram of the instrumentation set-up is presented in Figure 2-12. For the spinning tip tests the rate of rotation was measured with a hand held Shimpo tachometer.

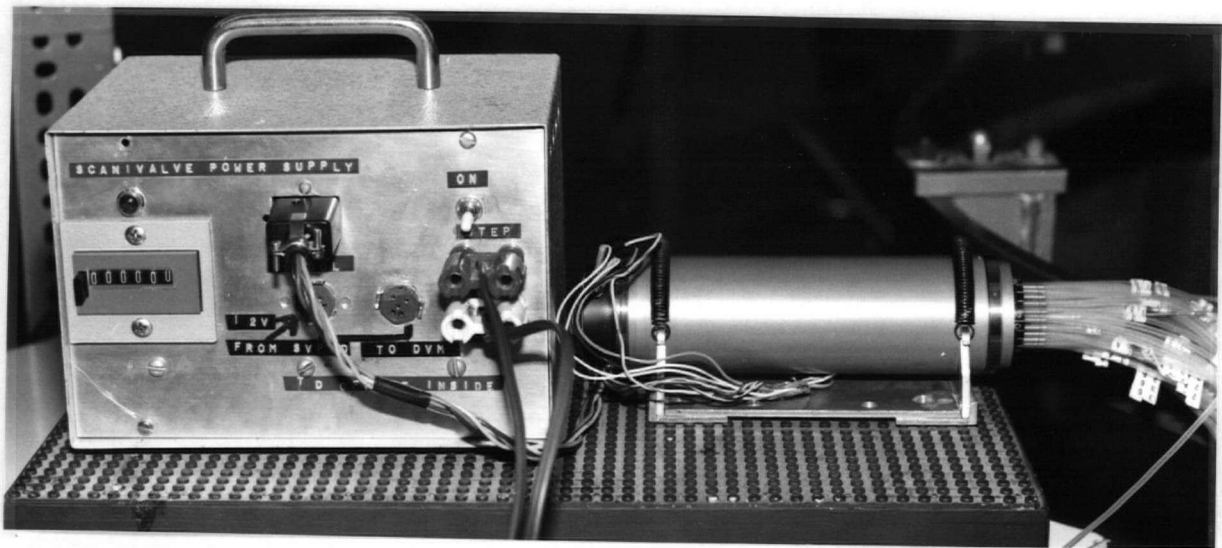


Figure 2-10 The scanivalve pressure line switching arrangement.

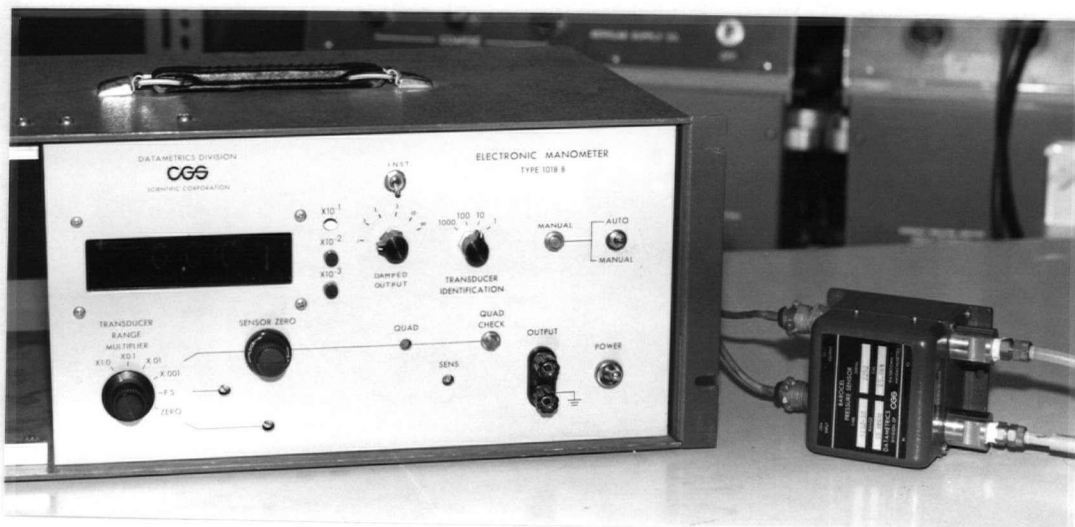


Figure 2-11 The Barocel pressure transducer and electronic manometer.

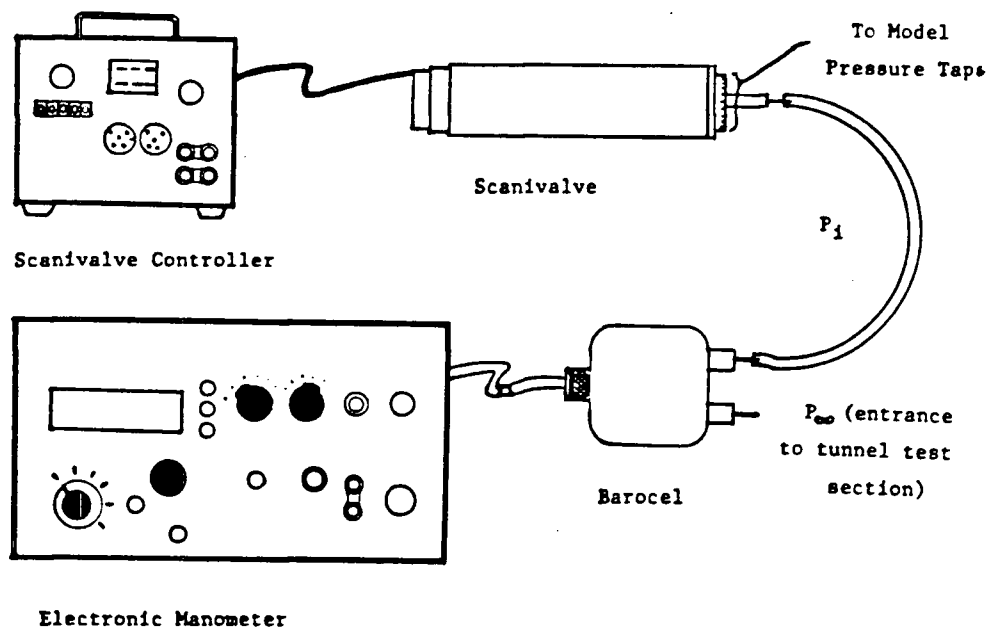


Figure 2-12 Instrumentation layout for pressure measurement using a Scanivalve and a Barocel Transducer.

## 2.5 Test Procedures

Earlier tests with a similar model [13] had indicated a need for a stronger model support as it was found to be susceptible to vibrations caused by highly turbulent separated flow at higher speeds and angles of attack. Preliminary tests with the improved support system delayed the onset of vibration to a  $> 50^\circ$  with the free stream speed as high as 25.8 m/s. Hence, for the present test program the wind speed was set at 22.7 m/s which (with one exception) eliminated vibration over the entire range of interest. This is more than double the speed previously achieved without vibration. The corresponding Reynolds number based on the maximum cone diameter is  $1.1 \times 10^5$ , which compares with that used by the earlier investigators [1,4,11,20] and hence facilitates comparison of the data. It is in the range where the Reynolds number

dependency is negligible and the flow separation is laminar. At a higher Reynolds number in the range of  $3 \times 10^5 - 2 \times 10^6$ , a laminar separation may still occur on one side while the flow on the other side may exhibit a laminar separation followed by a turbulent reattachment and separation. In this critical range of the Reynolds number much higher levels of side force have been reported, however, as pointed out before, the results have been less predictable and repeatable. It should be emphasized that the repeatability problem here is distinctly different in origin from that associated with the roll orientation.

The series of steps during a typical test may be summarized as follows:

- i) set the balance table to  $\alpha = 0$ ;
- ii) set the yaw angle  $\beta$  as desired;
- iii) set the nose tip to the required roll angle  $\phi$ ;
- iv) set the tunnel to a preselected wind speed;
- v) read pressures at the taps with the Scanivalve and the electronic manometer;
- vi) increase the angle of attack  $\alpha$  by  $10^\circ$  up to  $50^\circ$ , resetting the tunnel speed if needed.

Once the repeatable character of the data was established through a series of tests, the above procedure was shortened and the measurements were limited to  $\alpha = 30^\circ$ ,  $40^\circ$ , and  $50^\circ$ .

During the assessment of roll angle effects with the standard tip, the whole model was rotated about its axis as the tip could not be rolled independently. For the smaller spinable tips only the tip position was

changed. This is expected to give results similar to those obtained with the rolling of the entire body as shown by Keener et al. [21].

The dynamic head  $q = (1/2)\rho V_\infty^2$  and individual  $P_i - P_\infty$  pressure readings being available from each tap, a pressure coefficient can be obtained directly,

$$C_{pi} = (P_i - P_\infty)/q.$$

The pressure coefficients were integrated over the cone surface to obtain the force coefficients. The integration routine is summarized in Appendix I.

### 3 RESULTS & DISCUSSIONS

The amount of information obtained through a planned variation of the system parameters such as the tip geometry; roll, yaw and pitch angles; tip rotation; scanning of 40 pressure taps and their integration; etc., is rather extensive. There are several options available for the presentation of data. An effort is made to convey the information as concisely as possible with an emphasis on discernable trends.

The standard cone-tip data are presented first, which serve as reference to assess effectiveness of other tip geometries. The results with the nose-boom, delta-strake and porous tip follow. Finally, the effect of the tip rotation is evaluated. Such carefully planned experiments with repeatable results, aimed at side force alleviation through adjustment of the tip geometry are not reported in the literature.

#### 3.1 Standard Cone Tip Roll Tests

The plain cone tip (Figure 2-4) of 4:1 length to radius ratio was tested in the range of angle of attack from 0 to 50° in 12 different roll positions. The pressure coefficient at each pressure tap was calculated and integrated over the cone surface to evaluate the side force and normal force components. For both symmetric and asymmetric flow patterns the pressure distribution varied only slightly in the axial direction, i.e. from the nose to the base of the cone. On the other hand, large pressure variations were noticed in the circumferential direction especially for the asymmetric flow situations. Thus, a plot of pressure variation at any particular axial station can serve as a

qualitative pressure loading for the entire cone. The axial station P at 25.3% of the total cone length was selected to this end as it had the largest number of pressure taps.

Figure 3-1 shows a typical  $C_p$  plot for zero roll angle. In general the lift increases with an increase in the angle of attack. Note, in the range  $\alpha = 0 - 30^\circ$ , the circumferential pressure distribution at the station P is essentially symmetric about the axial vertical plane. The asymmetry appears at  $\alpha = 40^\circ$  suggesting the presence of a net side force. Figure 3-2 shows a similar asymmetric pressure distribution case, for a roll angle of  $300^\circ$ , but now the net side force is in the opposite direction. For the twelve roll positions tested the side force at a given angle of attack changed direction without suggesting any trend (with respect to the roll angle). This is understandable as the boundary layer instability is governed by the tip surface roughness, a random parameter.

Figure 3-3 presents the side force variation for 12 different roll positions. It clearly shows a large increase in side force starting at a close to  $30^\circ$ . This is approximately the value of the cone angle and compares well with the results of other investigators [1-5, 11, 12, 15, 17, 20, 21]. It is apparent that the side force changes direction rather randomly as explained before. Its magnitude for a given  $\alpha$  is also affected, perhaps due to the extent of asymmetry in the flow, induced by the surface roughness at the tip. This would require more extensive instrumentation to analyse the flow field accurately.

Figure 3-4 shows the normal force coefficient variation for the twelve roll positions. Note the results show a marked scatter, at a

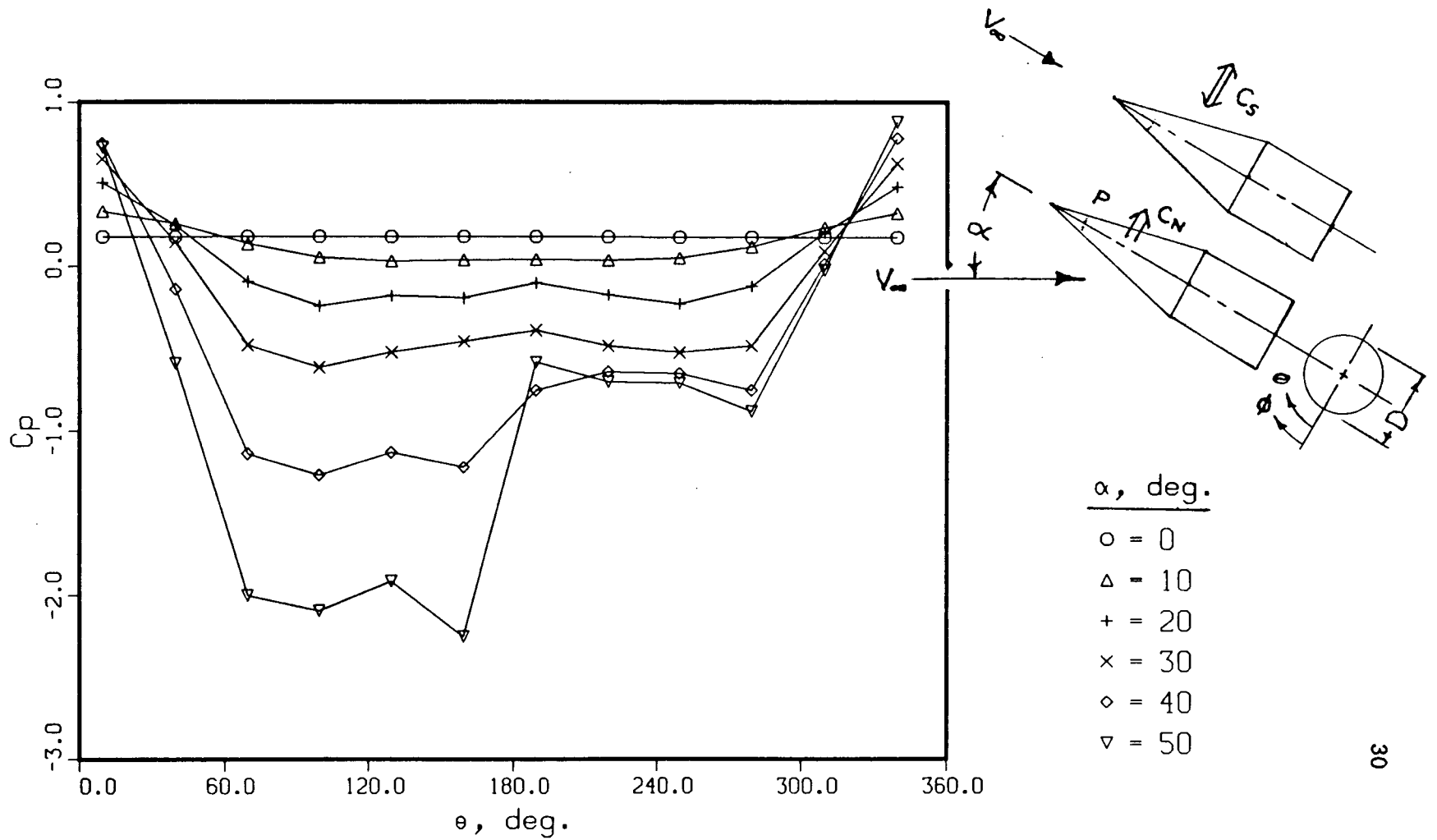


Figure 3-1 Pressure distribution at a reference station P, as affected by the angle of attack, for the standard tip at zero roll angle.

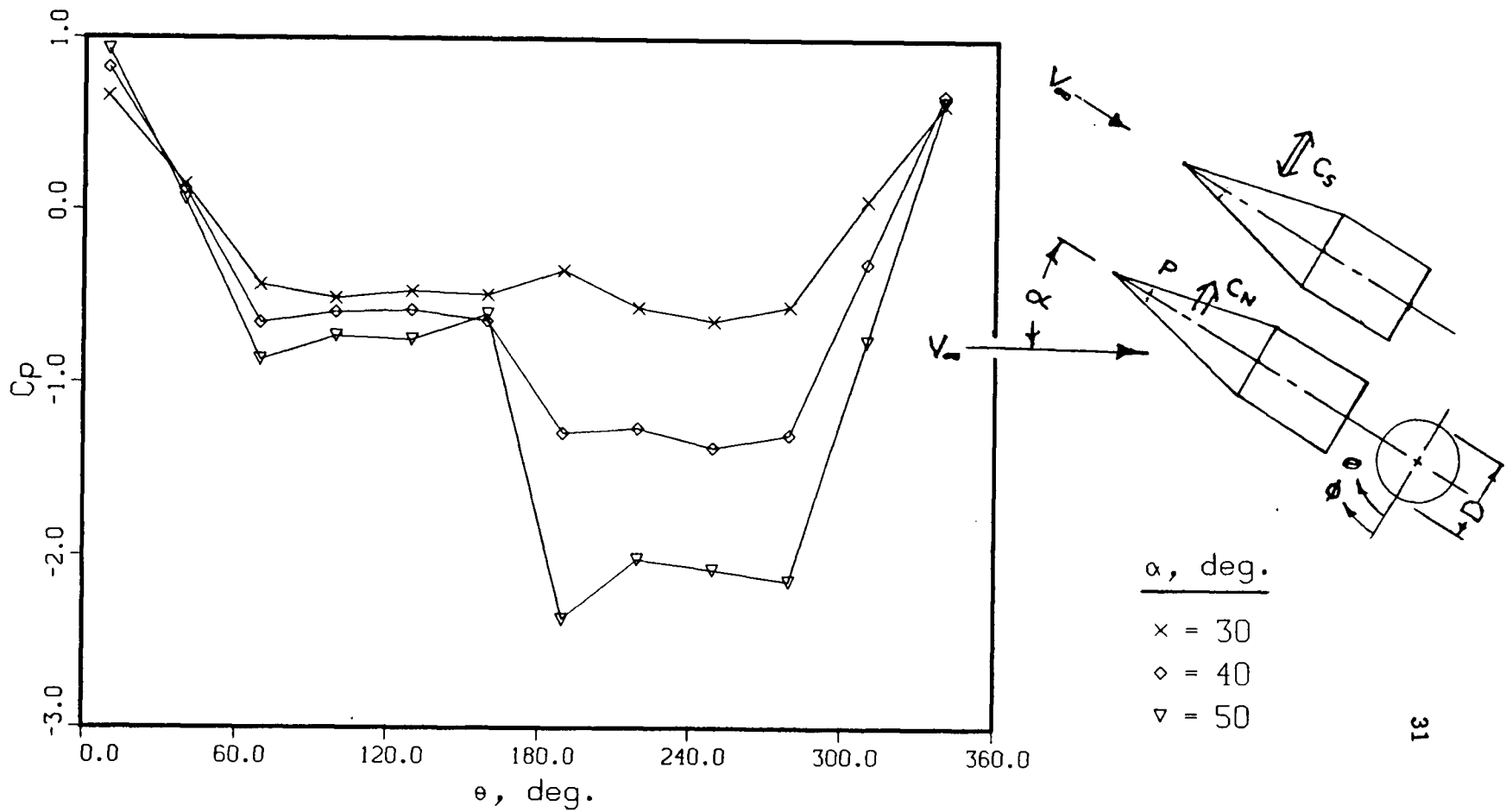


Figure 3-2 Pressure distribution at a reference station P, as affected by the angle of attack, for the standard tip at a roll angle of  $300^\circ$ .

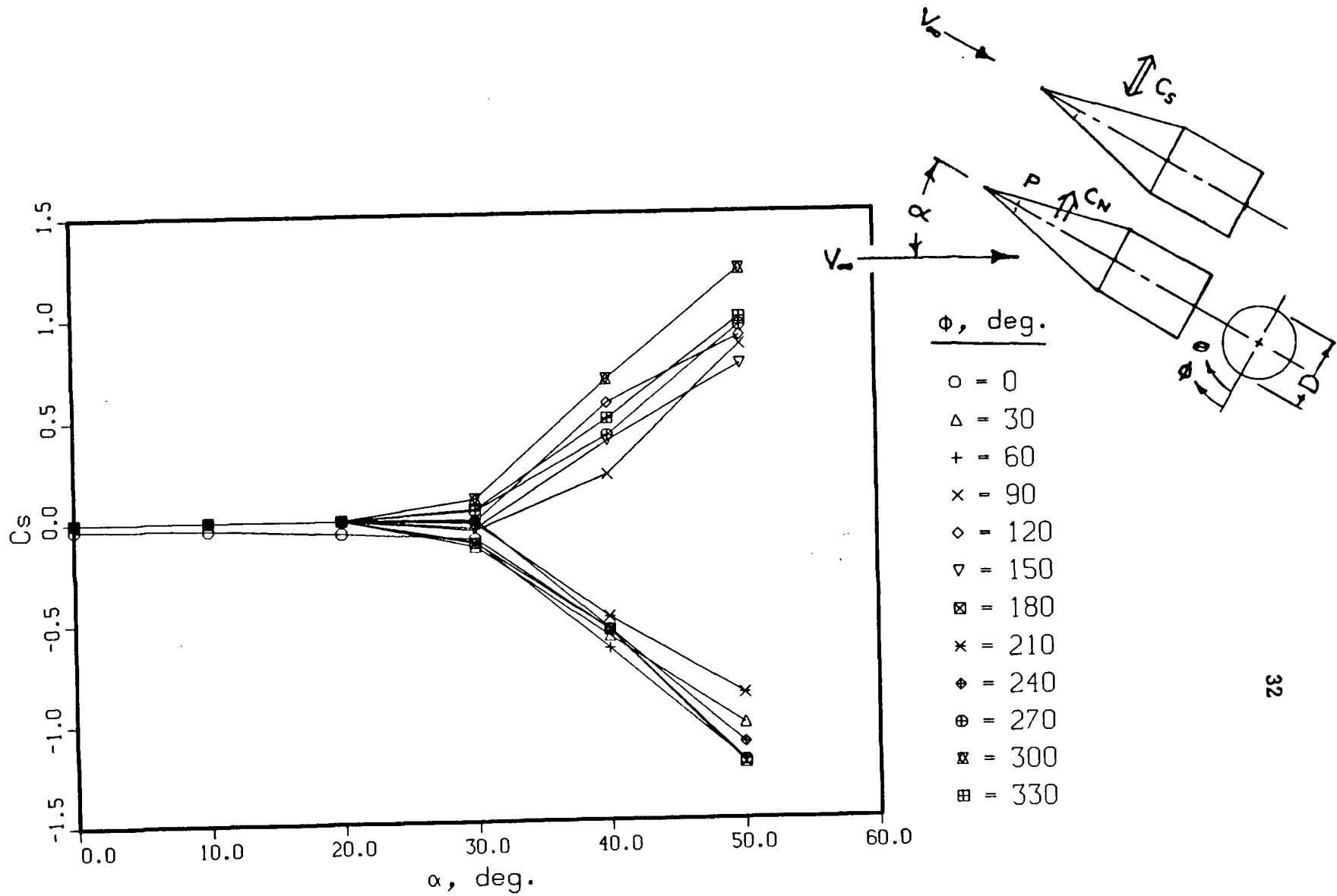


Figure 3-3 Variation of the side force coefficient for the standard tip model with pitch and roll.

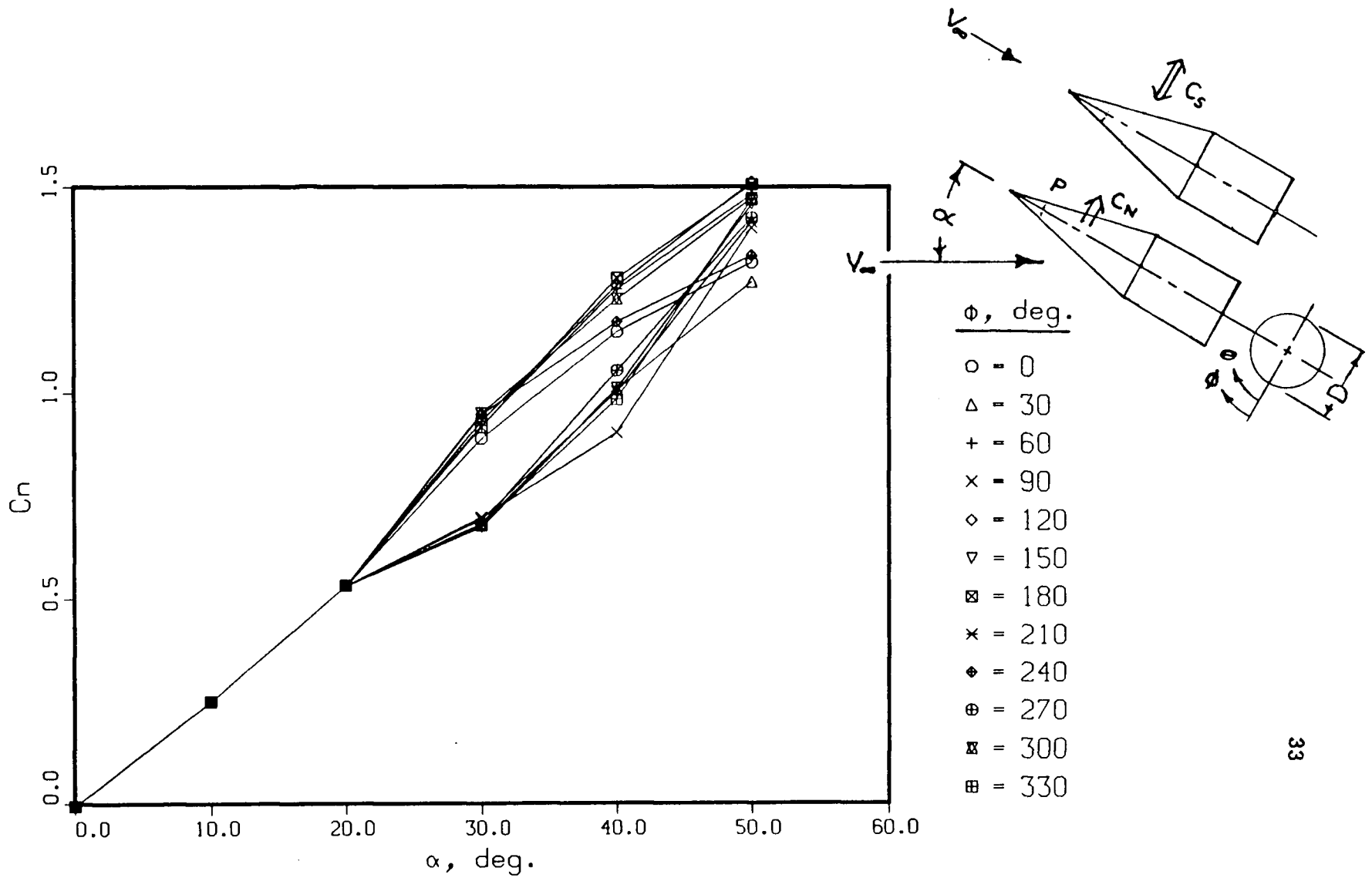


Figure 3-4 Variation of the normal force coefficient for the standard tip model with pitch and roll.

given  $\alpha$ , significantly larger than that observed for the side force. This can be explained by the flow field variations with the roll angle. Although the pressure plots of Figures 3-1 and 3-2 are repeatable and easy to integrate, the cone model is not covered with the same pressure tap density. Hence, the pressure integration over the cone surface can show some variation depending upon the orientation of the pressure taps. This was checked by integrating only the second ring of pressure taps (12 taps rolled through 12 positions). Now the normal force results showed distinctly less scatter. All subsequent tests were conducted at one body roll position, with the tip alone rotated to different roll positions. Thus the roll induced experimental error is eliminated in further tests.

Figure 3-5 shows the side force variation as affected by the roll position at a fixed pitch incidence of  $50^\circ$ . These results were obtained with the best polished and nearly symmetric nose tip. Note, the minor variations in the magnitude of the side force coefficient may be attributed to the pressure integration procedure as pointed out before. The effect of microasymmetry of the tip surface profile is strikingly visible. The side force variation follows a square wave type pattern similar to the one observed by Lamont [20]. The fact that Figure 3-5 shows two square waves discounts the probability of any large asymmetry in the model construction. Note, although the side force switches direction the normal force is nearly constant (Figure 3-6). The fluctuations in the normal force coefficient is entirely due to the roll induced pressure integration error. The model was rolled in steps of  $30^\circ$  while most of the pressure taps had a  $60^\circ$  spacing. This results in a positive or negative biasing of the result about its true value.

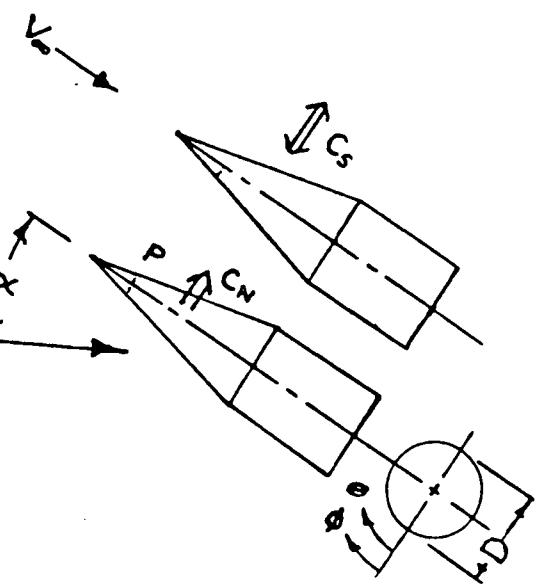
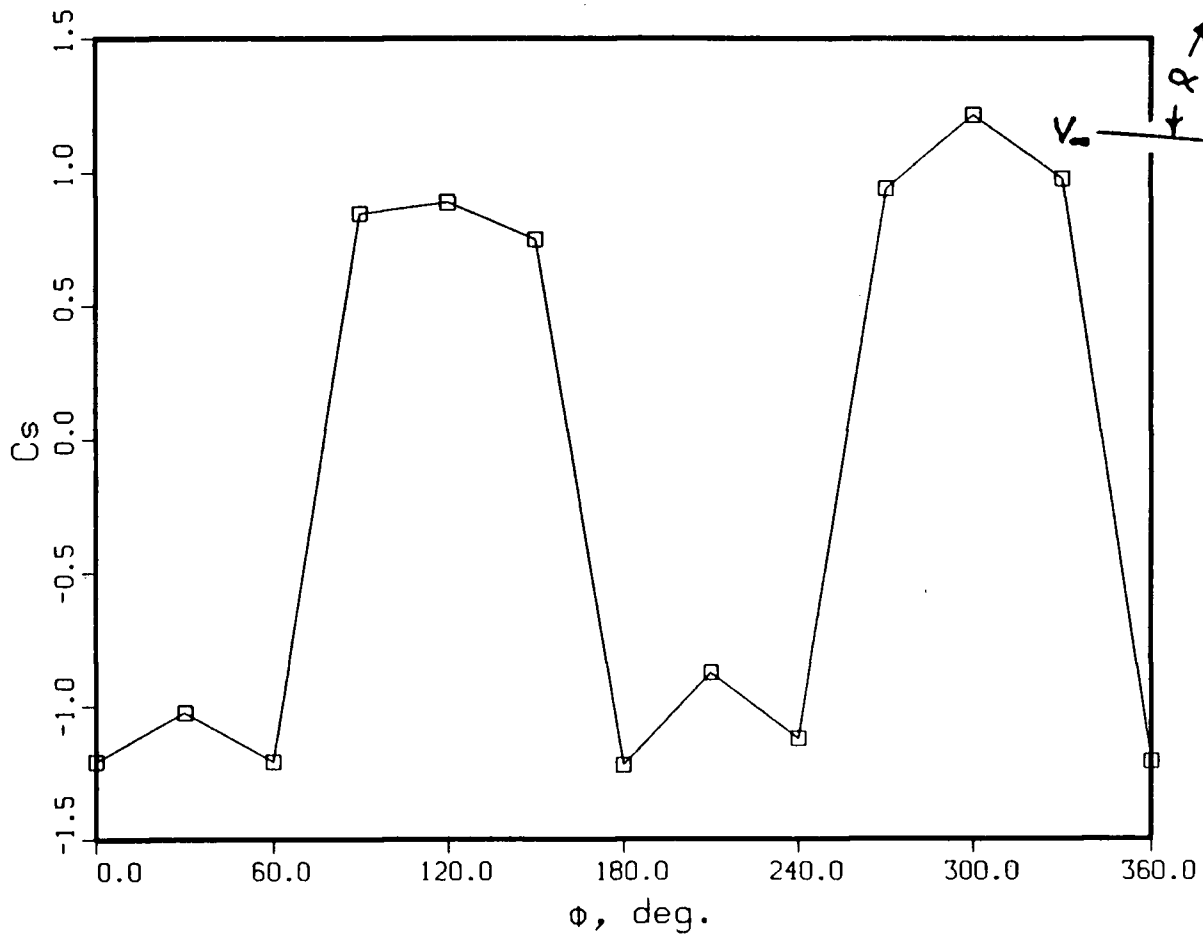


Figure 3-5 Effect of the standard tip roll position on the side force at a pitch angle of  $50^\circ$ .

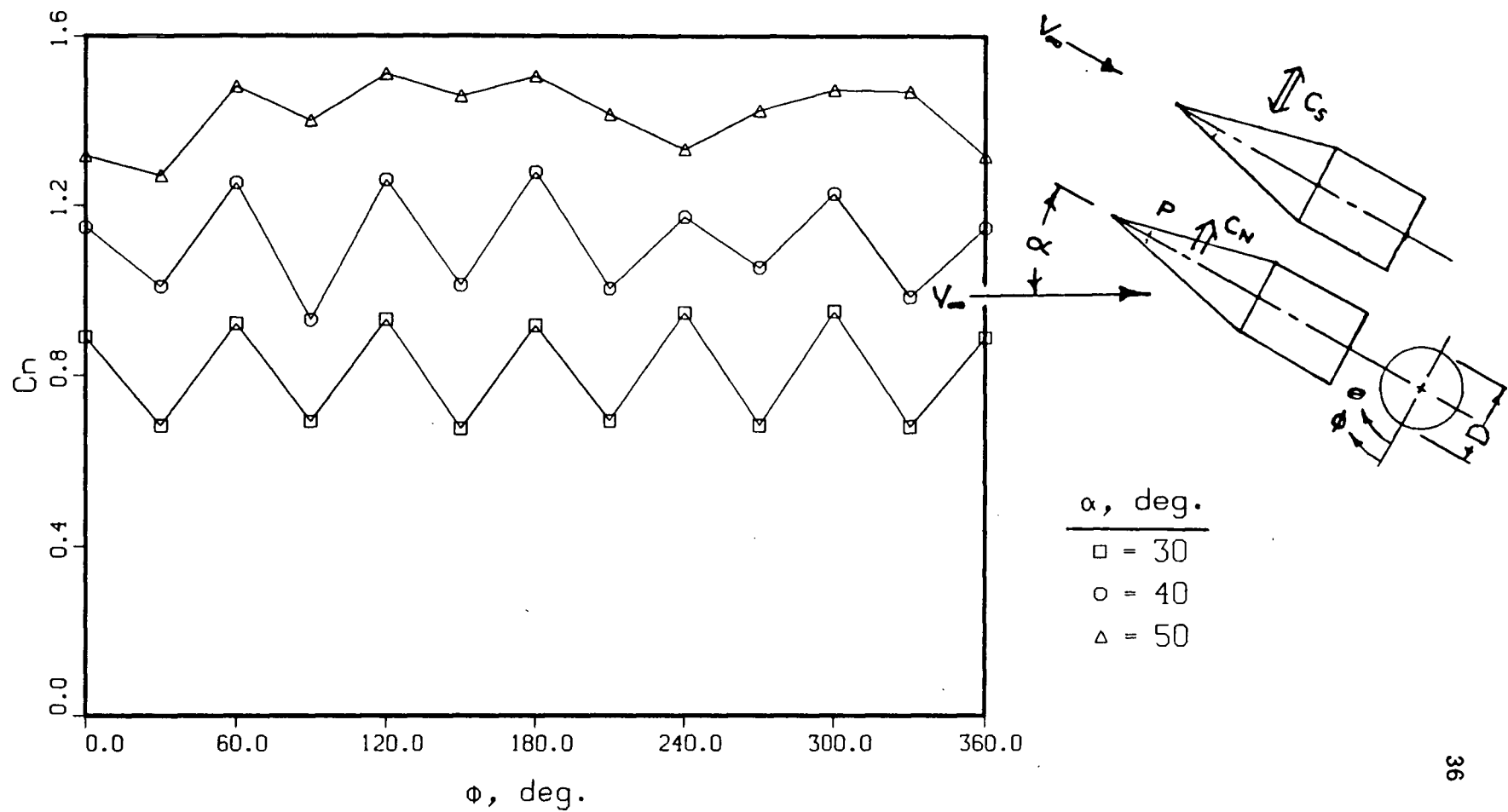


Figure 3-6 Effect of the standard tip roll position on the normal force.

The maximum recorded side force coefficient for the standard tip was 1.22. This is of the same order of magnitude as the normal force coefficient (1.5). This nominal value of the side force is used as a reference to assess the effectiveness of other tip geometries.

It may be pointed out that this nominal value of the side force coefficient compares well with that obtained by several earlier researchers. For example, Keener et al. [21] in his experiments with a 20° cone found  $C_s$  to be 1.25, while Viswanath and Narayan [11] obtained  $C_s = 1.10$  for a similar cone model.

### 3.2 Nose-Boom Tests

Each nose-boom was made from a 0.89 mm diameter tapered darning needle. A family of nine different needles, varying in length ( $L_b$ ) from 4.13 cm to 0.16 cm (4.13, 3.18, 2.54, 1.91, 1.27, 0.95, 0.64, 0.32, 0.16 cm) was used in this test-program.

Each test with a nose-boom was carried out at six roll positions. In these tests just the tip was rolled instead of the entire cone body. As pointed out by Keener et al. [26], this is expected to produce the same effect as that obtained by rolling the entire model. The experiments did substantiate this observation.

Figure 3-7(a) shows the side force variation with the pitch incidence and the nose roll position when the tip is fitted with a 4.13 cm nose-boom (the longest used in the test-program). A marked dependence on the tip roll orientation continues to be present at higher angles of attack ( $\alpha > 30^\circ$ ), similar to that observed with the standard tip. The magnitude of the maximum side force did show a significant

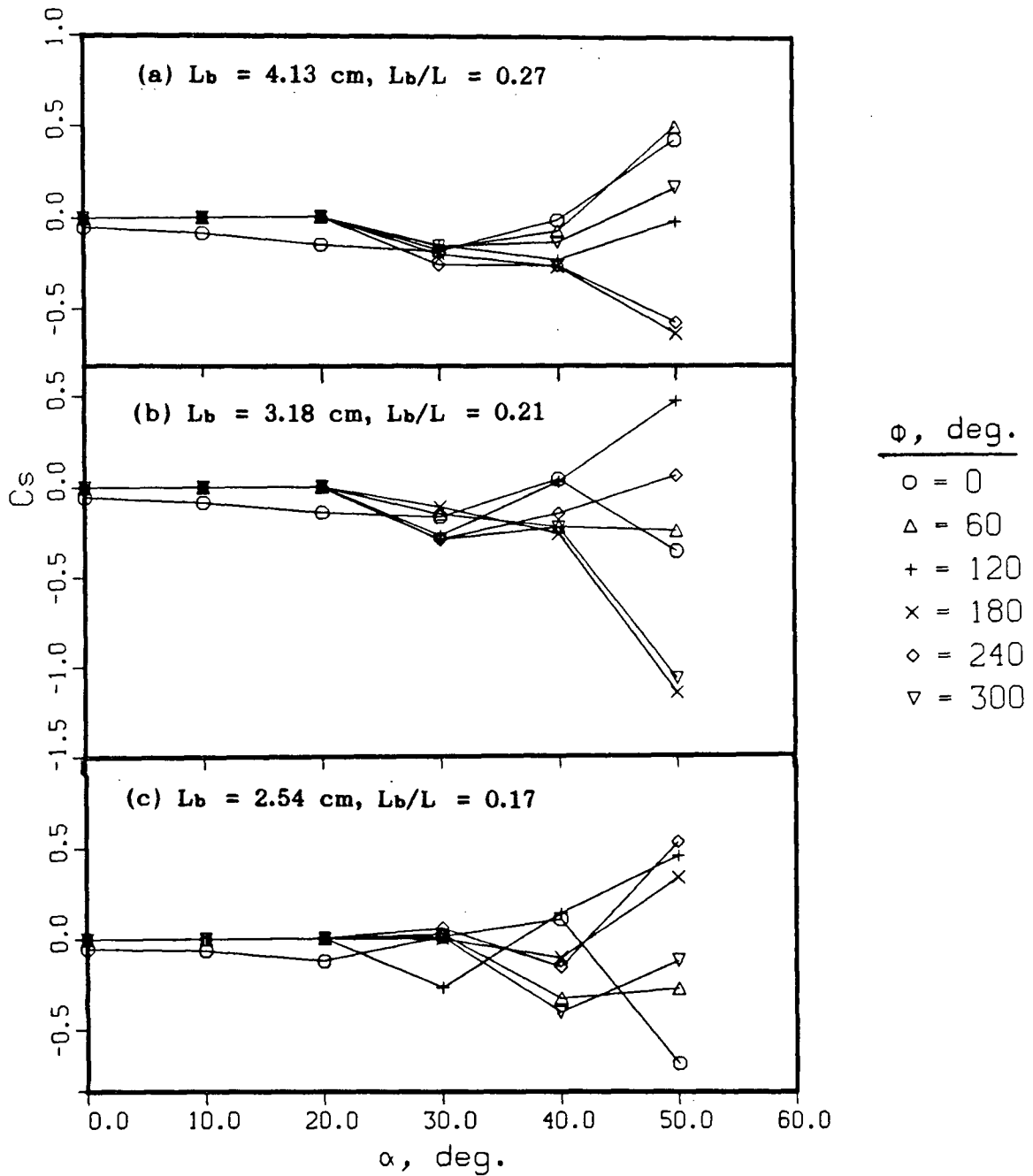


Figure 3-7 Effect of boom length on variation in the side force coefficient with pitch and roll attitudes: (a), (b), (c).

(50%) reduction. In fact during this set of tests, the largest nose-boom did result in the maximum side-force reduction.

Figures 3-7(b) to 3-7(i) show similar variations in the side force coefficient for the other nose-booms tested. The booms larger than 0.95 cm showed a reduction in the side force while those smaller than 0.95 cm showed an increase in  $C_s$ . It is of interest to note that the direction of the side force is dependent on both the pitch angle and the roll orientation.

In general, the changes in magnitude accompanying the changes in direction, with  $\alpha$  and  $\phi$ , were larger for shorter boom-lengths ( $L_b < 0.95$  cm).

It is important to point out that even for identical test conditions, i.e. for a given model at fixed pitch and roll orientations, and a fixed Reynolds number, repeating the test may lead to a different direction of the side force (without affecting its magnitude). This bistable character of the phenomenon is understandable considering its sensitivity to the free stream turbulence character, as well as the surface roughness distribution.

Figure 3-8 summarizes the above information in a useful way to better appreciate the effect of nose-boom and its length. It shows variations of the absolute maximum side force coefficient and its percentage change (from the no nose-boom case) as affected by the boom length. Although the local variations do not exhibit any well defined pattern the overall trends are well established. The shorter boom lengths ( $L_b/L < 0.7$ ) tend to increase the side force, however, for longer boom lengths there is a distinct reduction in the maximum  $C_s$ . It

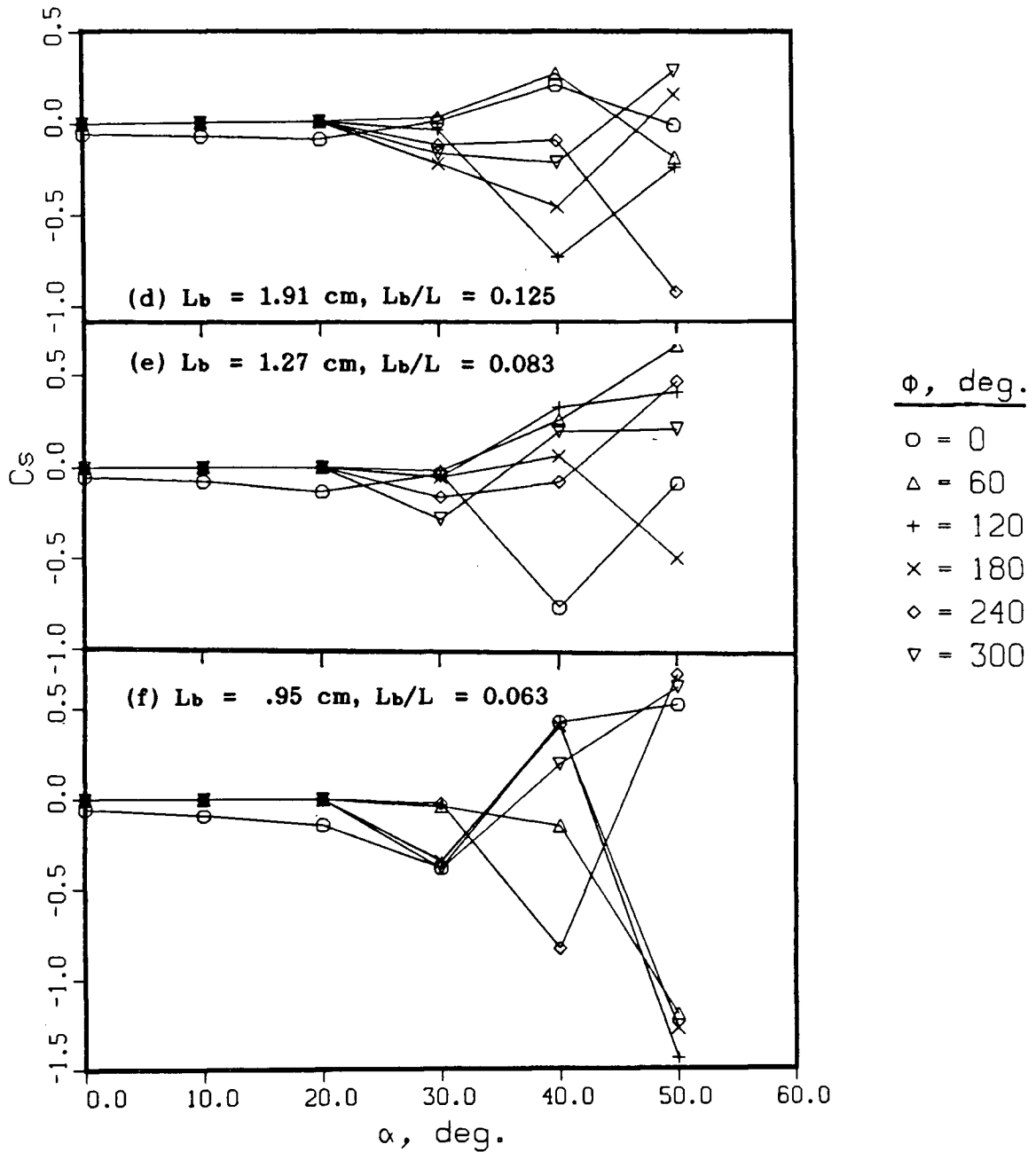


Figure 3-7 Effect of boom length on variation in the side force coefficient with pitch and roll attitudes: (d), (e), (f).

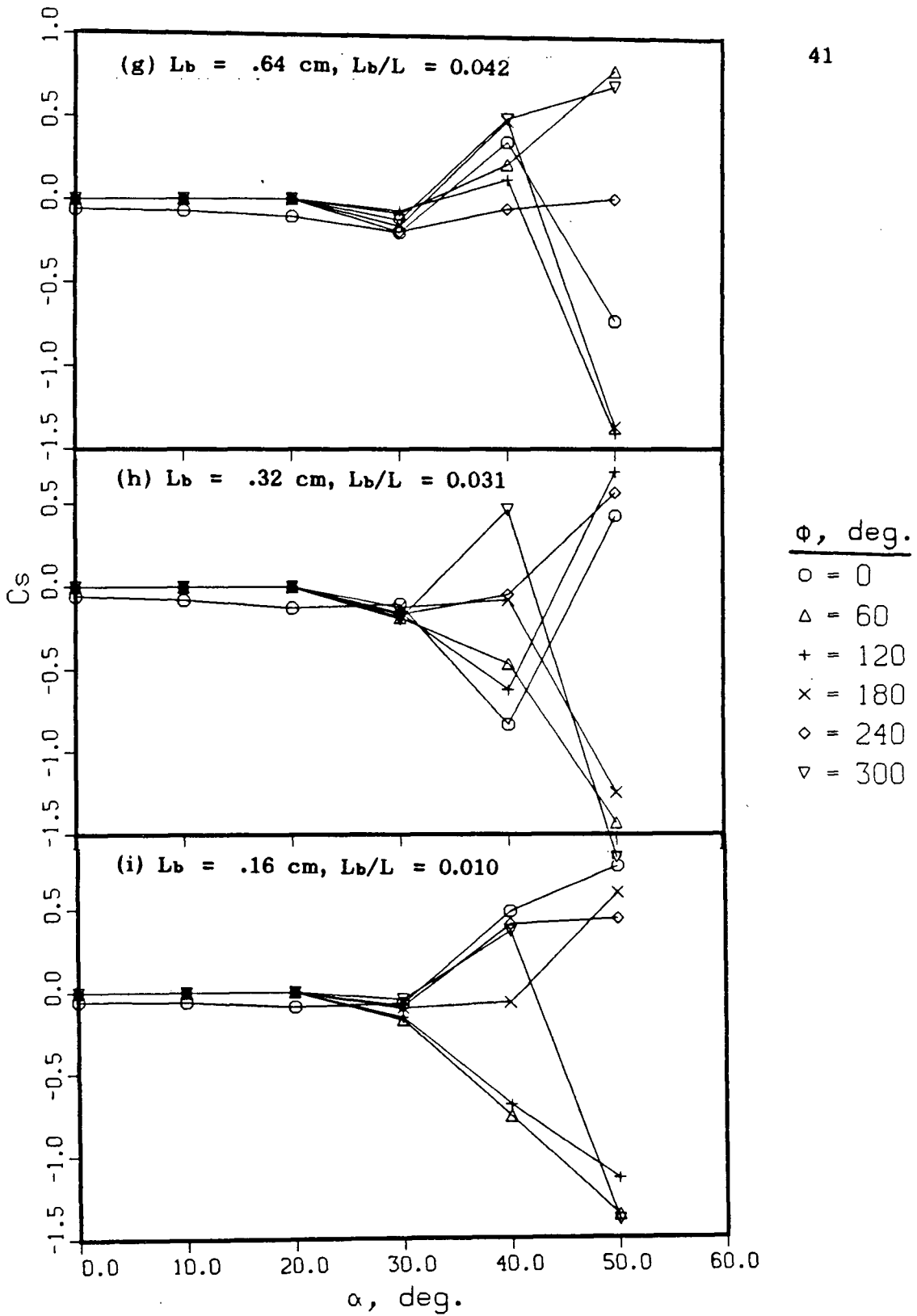


Figure 3-7 Effect of boom length on variation in the side force coefficient with pitch and roll attitudes: (g), (h), (i).

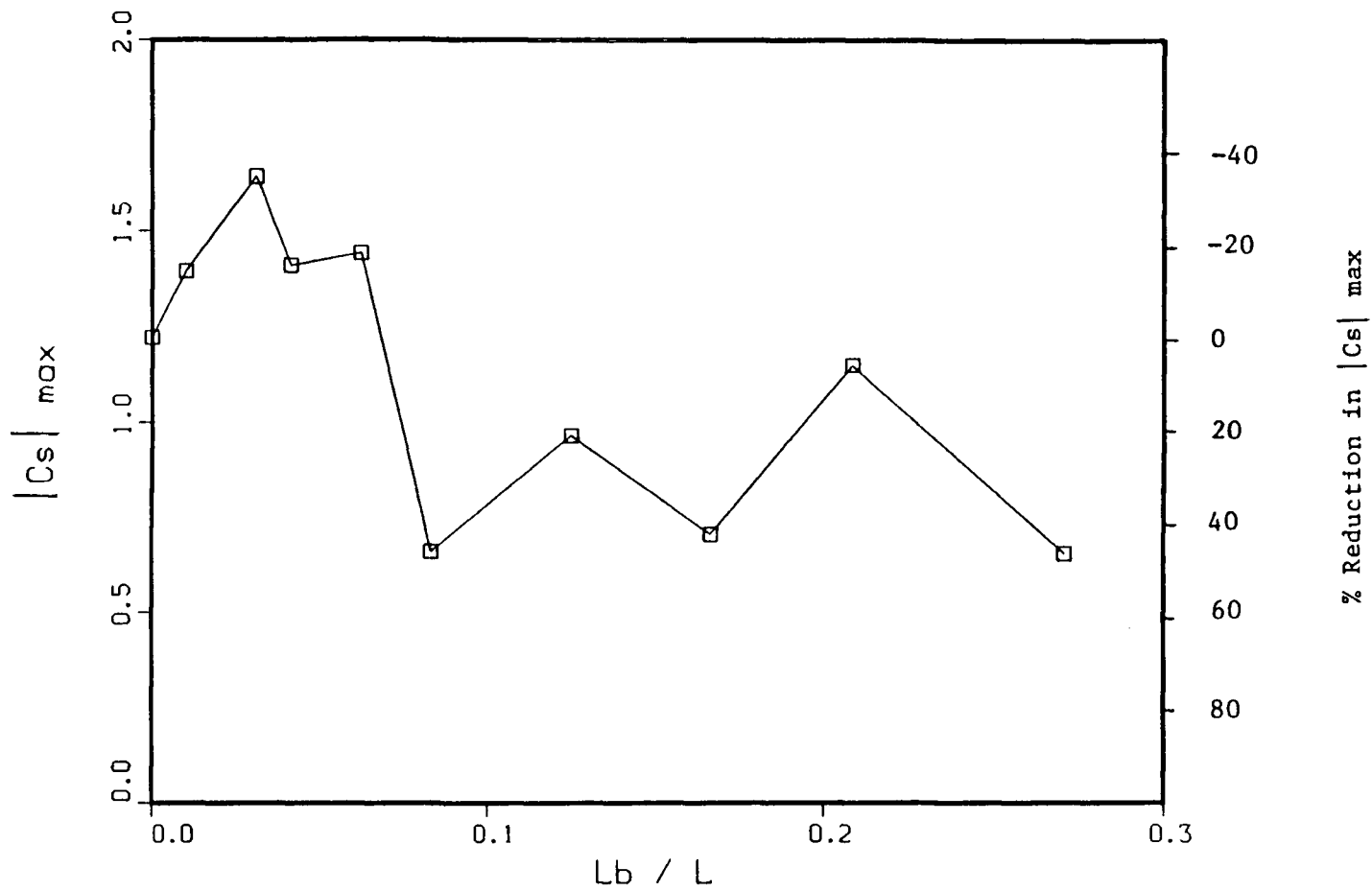


Figure 3-8 Magnitude of the maximum side force coefficient with varying nose-boom length including the standard tip case.

is possible to achieve a reduction in maximum side force coefficient by around 50% through the appropriate choice of the nose-boom length.

Figure 3-9 shows normal force variations with the pitch angle for the case of a 4.13 cm nose-boom. It is nearly linear with little scatter. The normal force plots for the other boom lengths show similar trends. Variation of the normal force with the nose-boom length is shown in Figure 3-10. It is apparent that effect of the boom length on the normal force coefficient is relatively small.

### 3.3 Delta Strake Tests

Tests with 3.18 cm delta strake tip shown in Figure 2-8 were conducted at 6 different roll positions. Of primary interest was the effect of the strake when perpendicular to the pitch plane, as this configuration was expected to be successful at minimizing the side force. However, the tests were also conducted at roll angles of  $\pm 10^\circ$ ,  $\pm 20^\circ$  and  $90^\circ$ . The small roll angles would be of interest for noncoordinated flight maneuvers, while the  $90^\circ$  position was tried to compare its effectiveness in side force alleviation with the more conventional orientations of the strake.

Results of the side force variation with pitch and roll attitudes for the 3.18 cm delta strake are presented in Figure 3-11. Note, both zero and  $90^\circ$  roll orientations of the strake seem to promote symmetric flow fields with the zero position proving a little better. For a given pitch angle, particularly with  $\alpha \geq 30^\circ$ , the presence of a small roll angle ( $\pm 10^\circ$ ,  $\pm 20^\circ$ ) seems to reduce effectiveness of the strake in promoting the flow symmetry. However, it is encouraging that the side force remains relatively low over the entire range of the pitch angle tested.

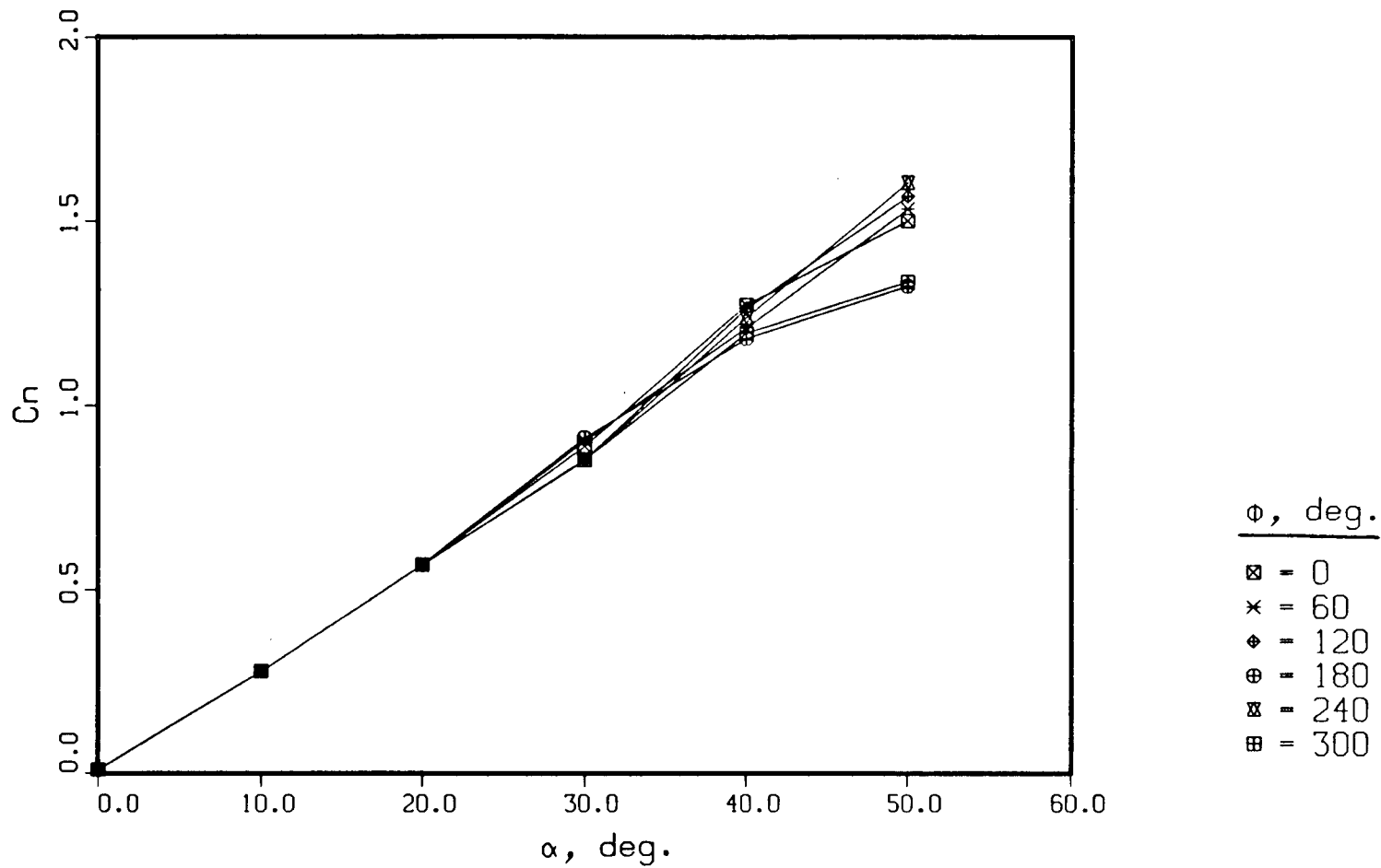


Figure 3-9 Normal force variation with pitch angle and roll orientation for the 4.13 cm nose-boom.

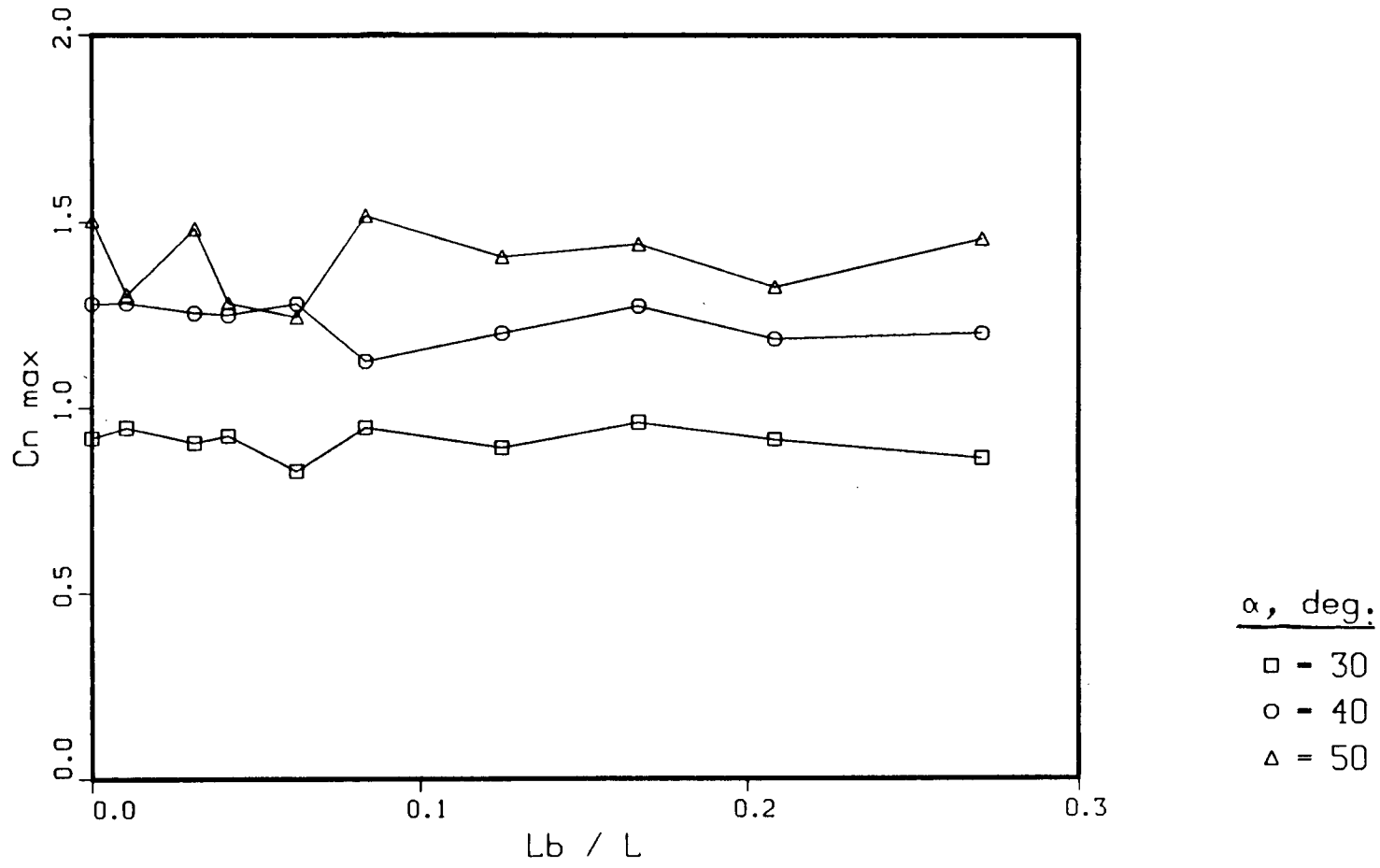


Figure 3-10 Normal force coefficient variation with pitch incidence and nose-boom length.

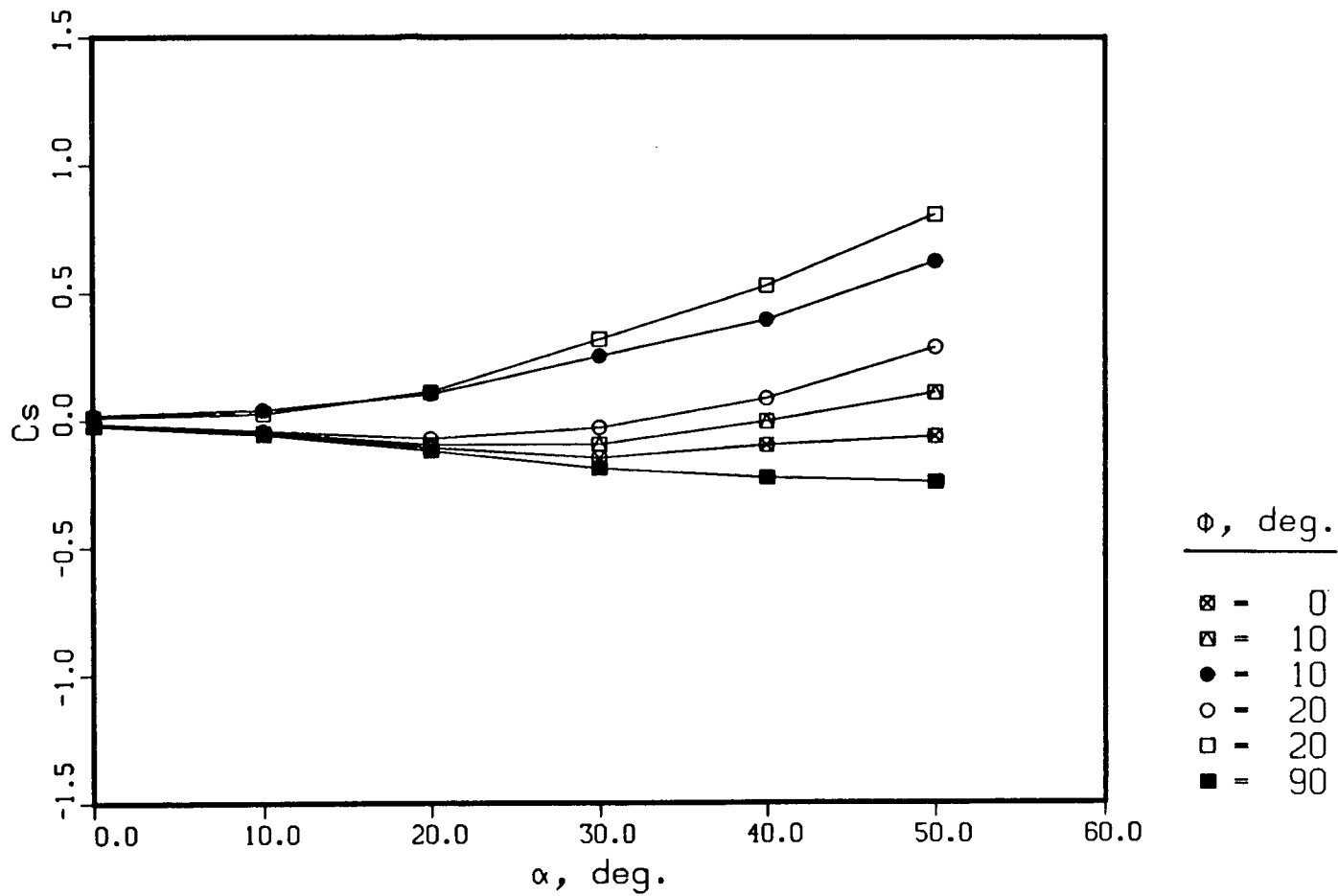


Figure 3-11 Variation of the side force coefficient with pitch and roll angles for the 3.18 cm delta strake.

As several investigators have reported a loss of lateral-directional stability with strake alleviation devices, it was deemed important to conduct tests at nonzero yaw angles as well as the normal zero sideslip condition. Pressure distribution plots over the cone surface with the standard tip, as affected by the pitch for  $\beta = \pm 10^\circ$  are presented in Figure 3-12. In Figure 3-12(a) the cone is yawed to the right (as viewed by the pilot). At zero angle of attack, the pressure distribution shows a clear side load to the right. However, as the pitch angle increases the side force reverses direction and is to the left. This suggests a strong positive stability. On the other hand, pressure plots for  $\beta = 10^\circ$  in Figure 3-12(b) show the reverse trend indicating a negative stability.

The resultant side force coefficients are plotted against the pitch angle for  $\beta = 0^\circ$  and  $\pm 10^\circ$  (Figure 3-13a) for the standard tip. In this series of tests it seems the side force direction is not affected by the yaw direction. It appears that microasymmetry of the cone tip surface easily overpowers any inherent directional stability of this forebody configuration.

Results for the pressure integrated side force data for the various lengths of delta strake tested are presented in Figures 3-13(b) through 3-13(g). Evidence of a weak but positive directional stability is apparent for the 3.18 cm strake tip (Figure 3-13g). It is of interest to note that the stability gets progressively weaker as the strake size decreases and below  $L_s = 1.27$  cm the model becomes increasingly more unstable in yaw.

It is important to point out that all the strake tips larger than 0.32 cm showed promise in terms of the side force reduction. On the

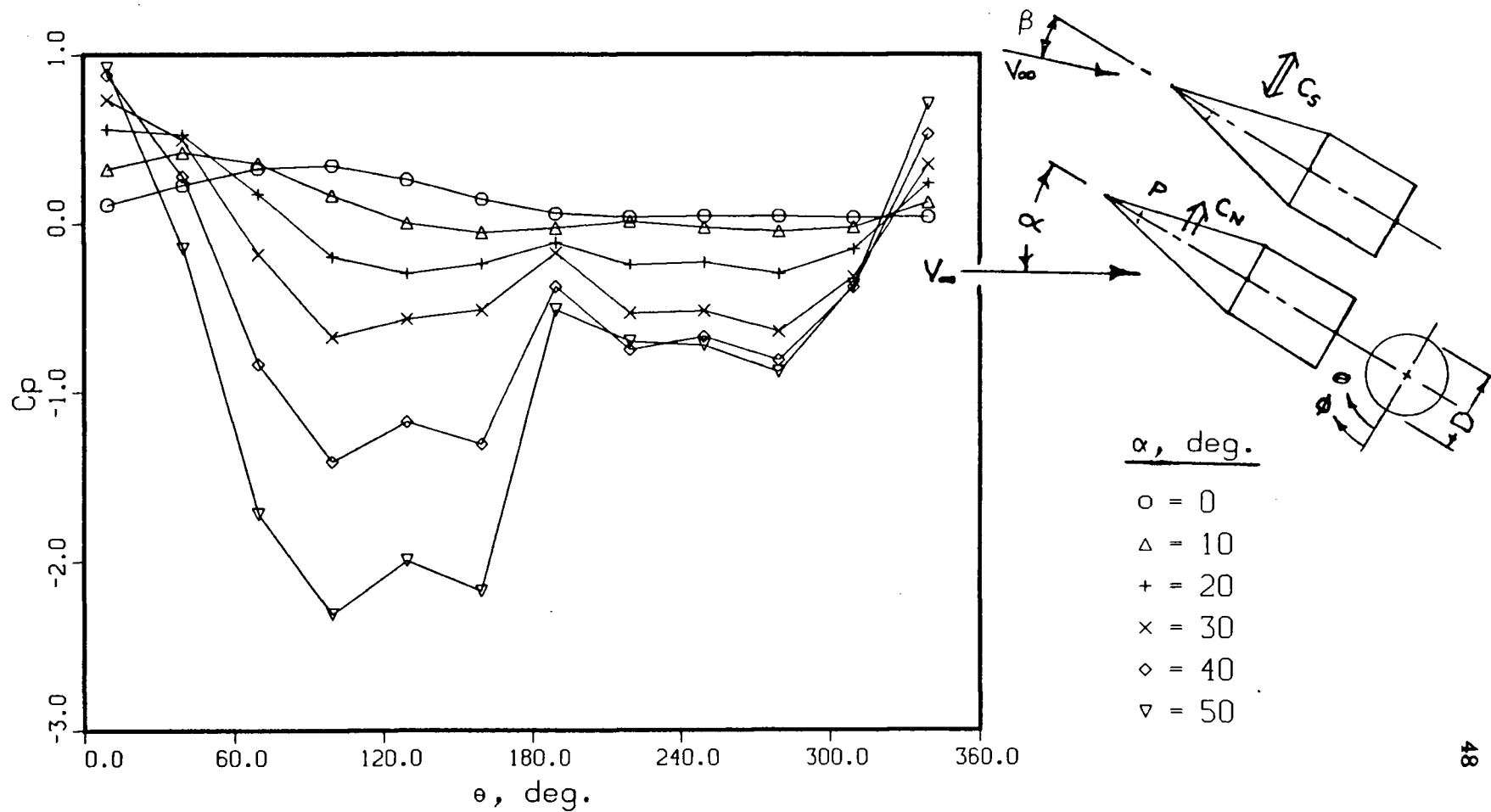


Figure 3-12 Pressure distribution, at the reference station P, for the standard tip at a yaw incidence of:  
 a)  $\beta = -10^\circ$ .

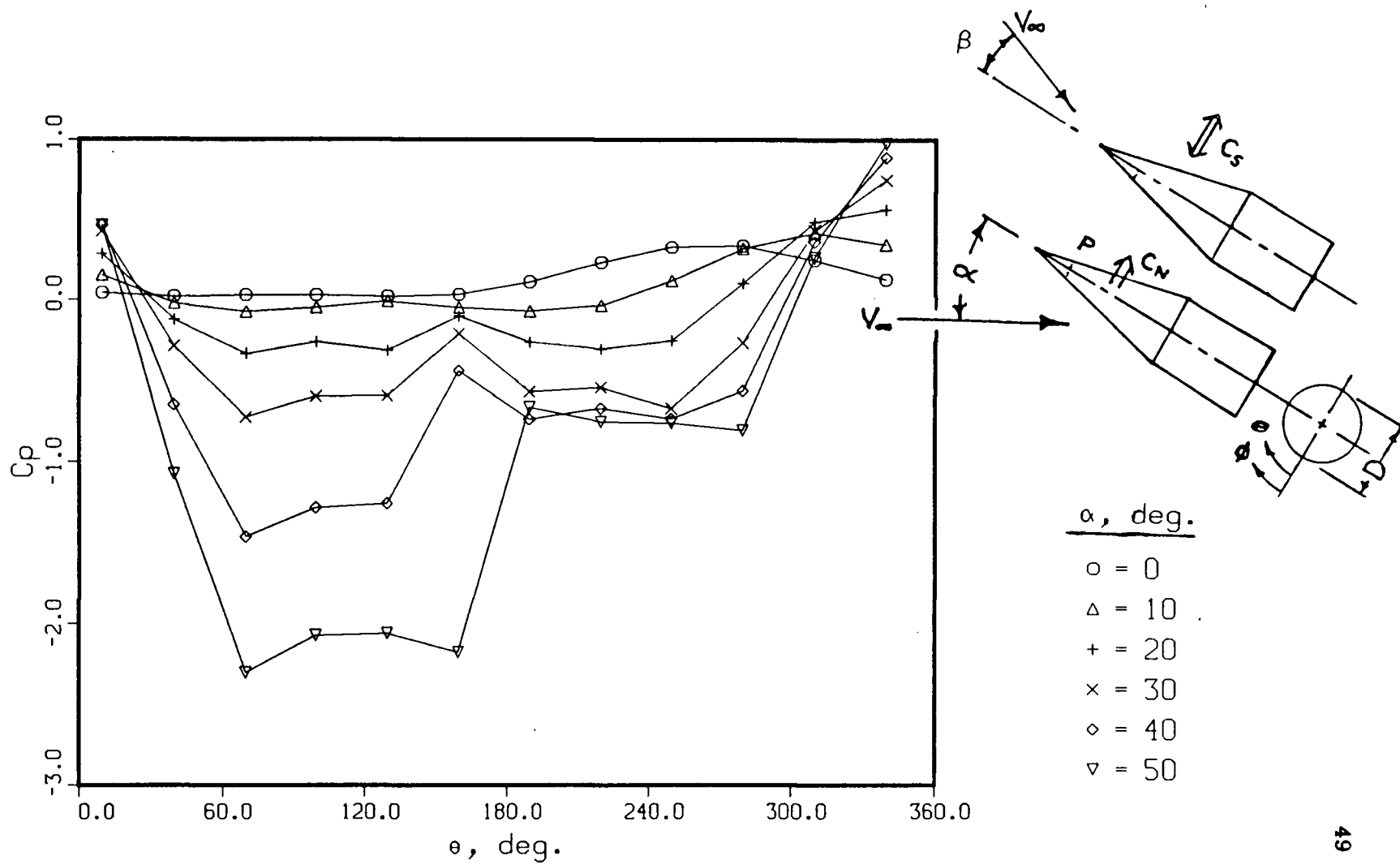


Figure 3-12 Pressure distribution, at the reference station P, for the standard tip at a yaw incidence of:  
 b)  $\beta = +10^\circ$ .

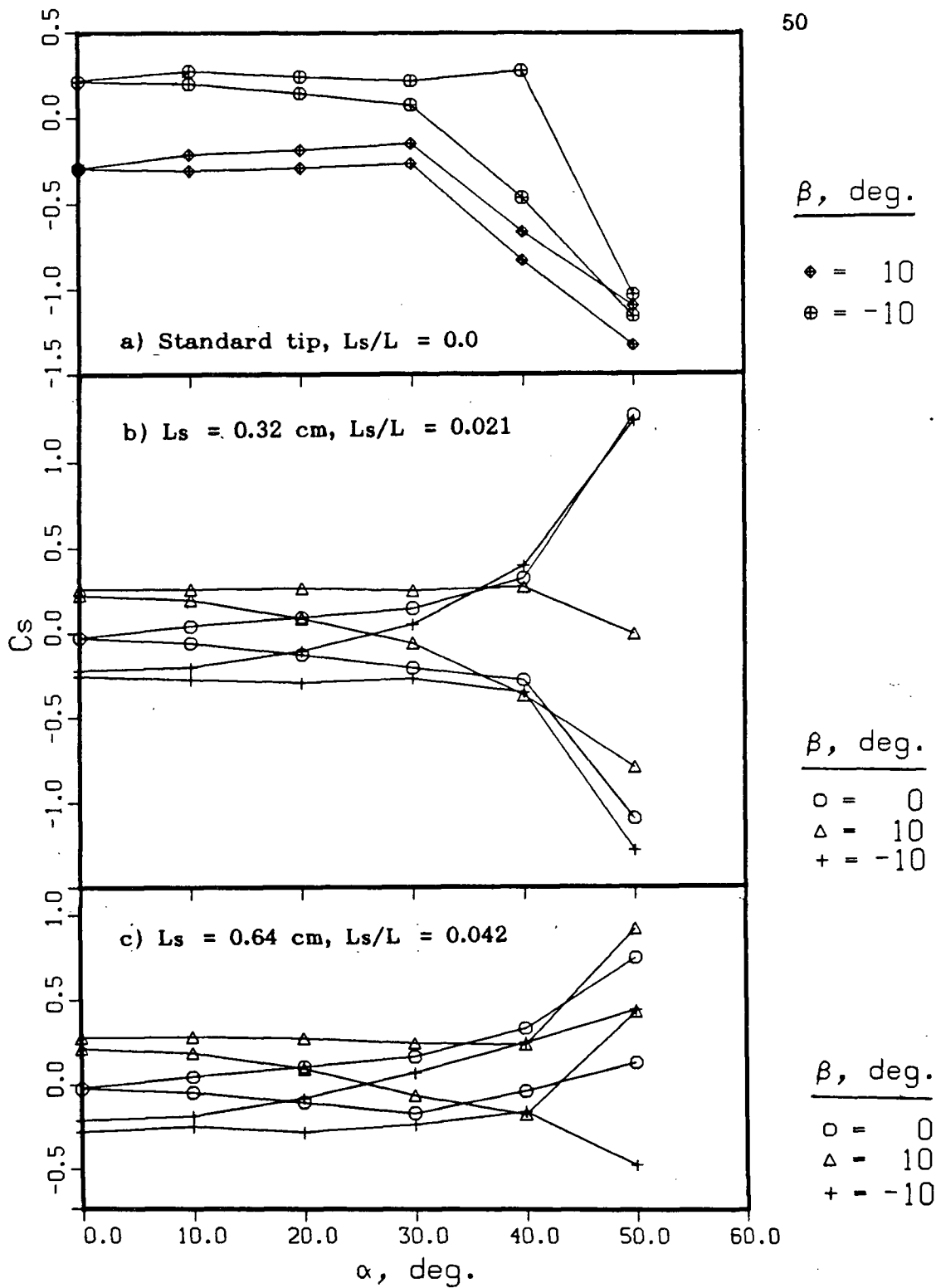


Figure 3-13 Variation of the side force coefficient with pitch and yaw angles as affected by the delta strake length (aspect ratio =1): (a), (b), (c).

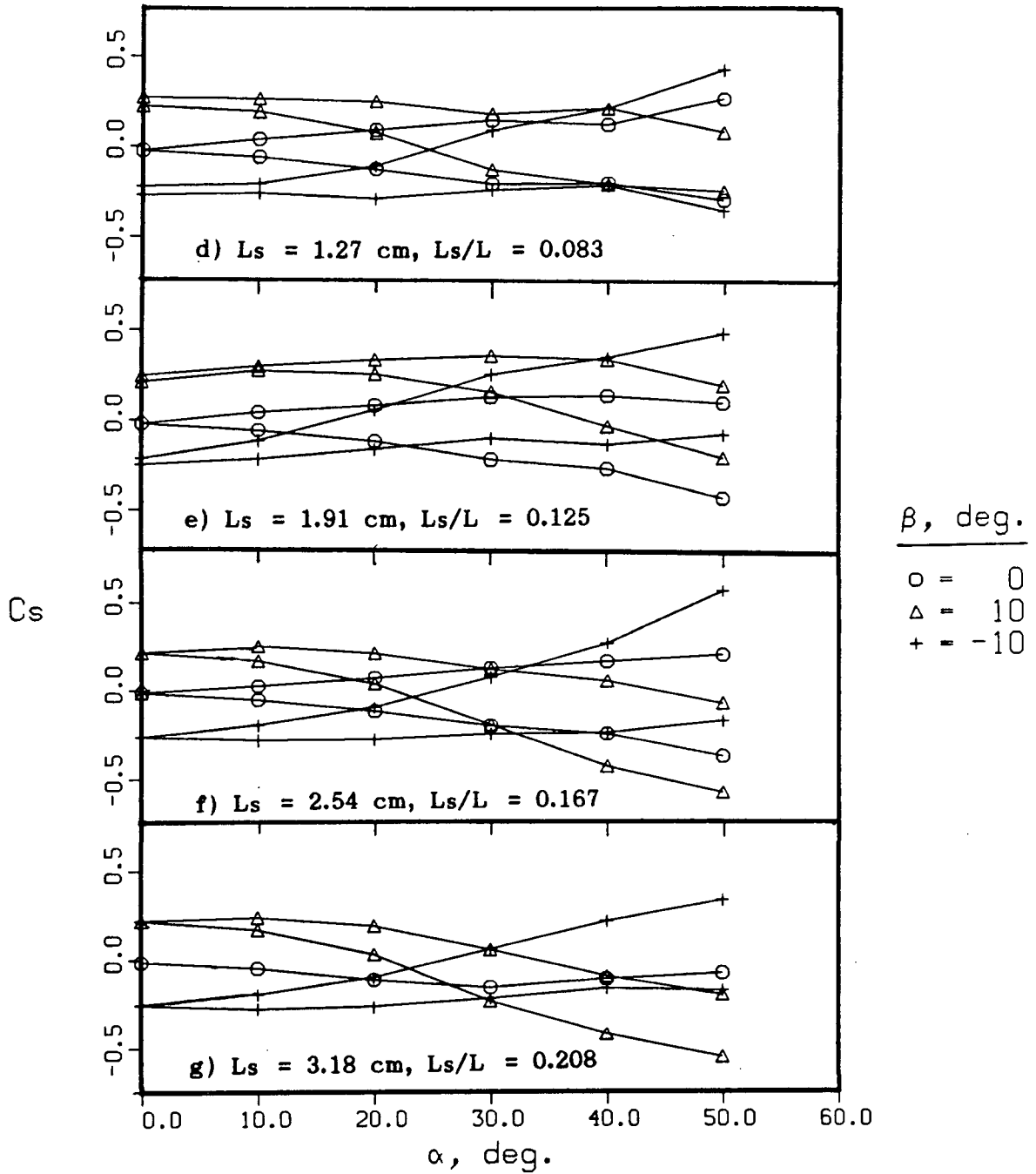


Figure 3-13 Variation of the side force coefficient with pitch and yaw angles as affected by the delta strake length (aspect ratio =1): (d), (e), (f), (g).

whole they performed much better than the nose-booms. The maximum reduction in the side force coefficient achieved was around 88% of the nominal value with the delta strake of  $L_s = 3.19$  cm (Figure 3-14).

As with the nose-boom study, the variation of the normal force with the pitch angle is essentially linear. However, the presence of yaw does tend to scatter the results at a given  $\alpha$ . Figure 3-15 shows the normal force coefficient results for the 3.18 cm delta strake as affected by pitch and yaw angles. Figure 3-16 summarizes the normal force results for the family of delta strakes. A slight decrease in the normal force is noted as the strake length is increased. If the forebody lift contribution is a significant portion of the total lift of a missile or an aircraft, then the importance of this loss of lift would have to be analysed. It seems, however, a small penalty to pay for the large reductions in the side force obtained with these tips.

#### 3.4 Porous Tip Tests

The porous brass tip used in the test program (Figure 2-5) was equipped with a 3.18 cm nose-boom, and perforated with 0.64 mm holes. The perforated portion comprised approximately 20% of the total cone length. The maximum recorded side force coefficient was 0.62, a 38% reduction from the nose-boom case and a 49% reduction from the standard tip value. On the other hand, the porous tip recorded a slightly higher (6%) normal force than that with the standard tip.

It seems logical that an efficient porous tip with near instantaneous communication of pressure across its surface would enhance symmetric vortex formation, as well as negate the effects of

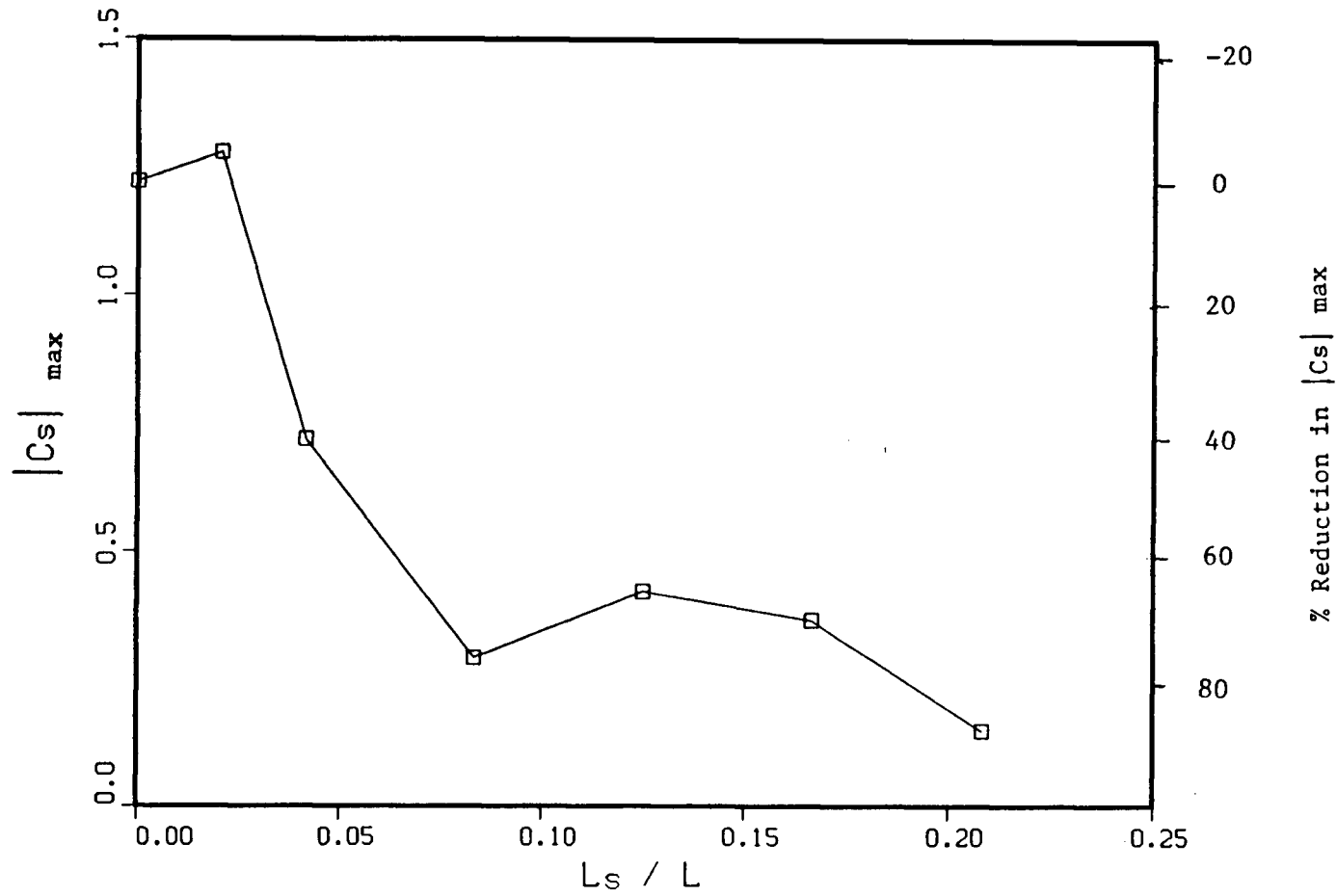


Figure 3-14 Effect of the stroke length on the magnitude of the side force.

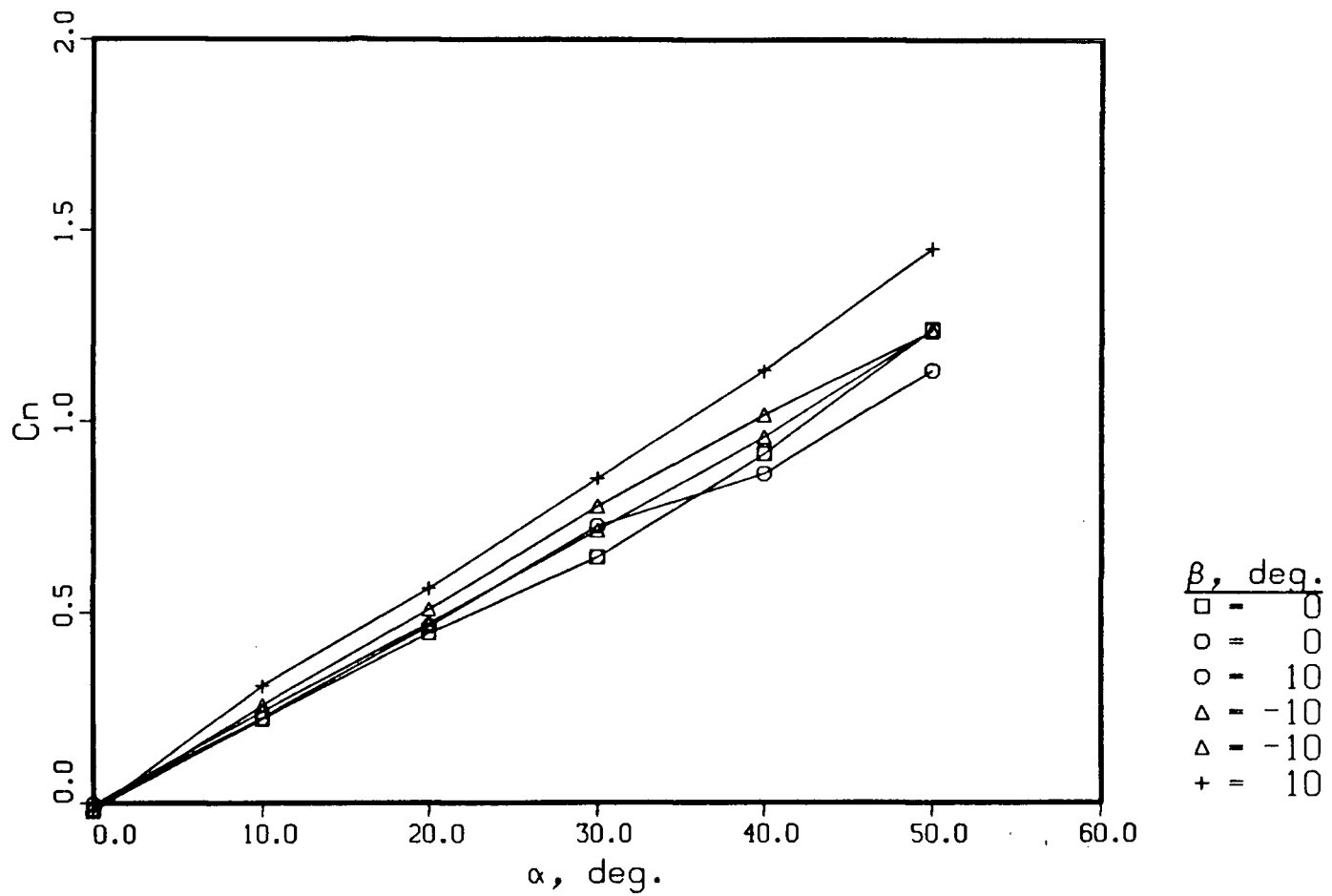


Figure 3-15 Variation of the normal force coefficient with pitch and yaw angles for a strake of 3.18 cm.

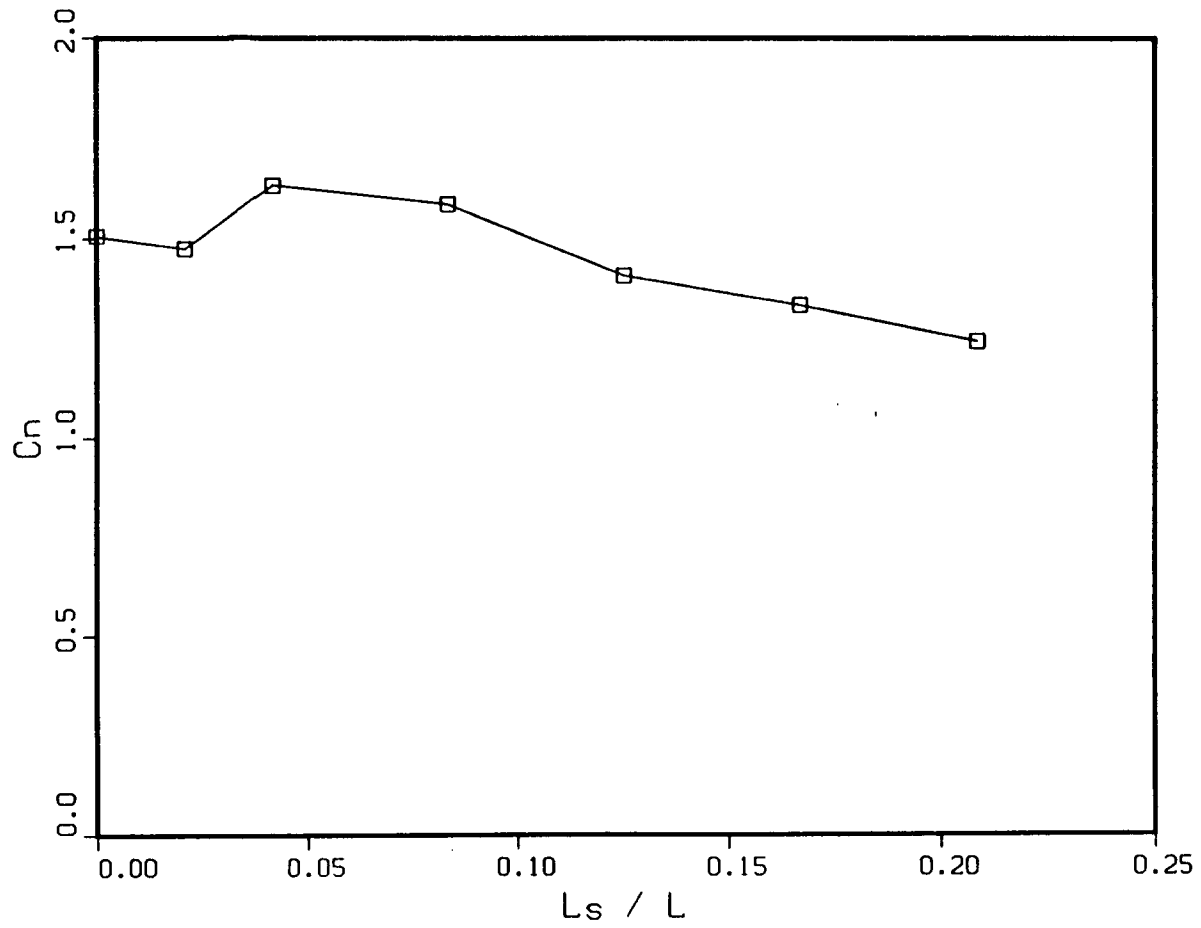


Figure 3-16 Effect of the strake length on the normal force coefficient.

asymmetric vortices. The porous tip used in the present test program had several limitations:

- (i) the tap size is rather large contributing to the surface roughness thus partly cancelling its desired influence;
- (ii) the porous length is perhaps too long, thus presenting a larger internal volume resulting in the average pressure that is different from the local value;
- (iii) the problem in (ii) is further accentuated here as the internal gap extends to the base of the cone and communicates with the pressure there.

However, effectiveness of the porous tip in reducing the side force is clearly established, even by this preliminary test. Better planned experiments in this direction are likely to be fruitful.

### 3.5 Spinning Tip Tests

The earlier preliminary investigation by Modi et al. [12] had suggested a possible reduction in side force when the tip of the cone was spun. Several carefully planned tests were conducted to assess more precisely the effect of tip rotation. The first set of tests involved spinning the standard tip and the nose-booms of up to 1.27 cm length. All these tests were conducted at 2000 rpm, the maximum speed of the small D.C. motor used. Variations in the side force with the pitch angle are shown in Figure 3-17. For each tip tested the model was pitched through to 50° and the test repeated with the spin reversed. Two observations of interest can be made:

- i) The direction of the spin determines the direction of the side force. A clockwise rotation leads to a net left side force (as

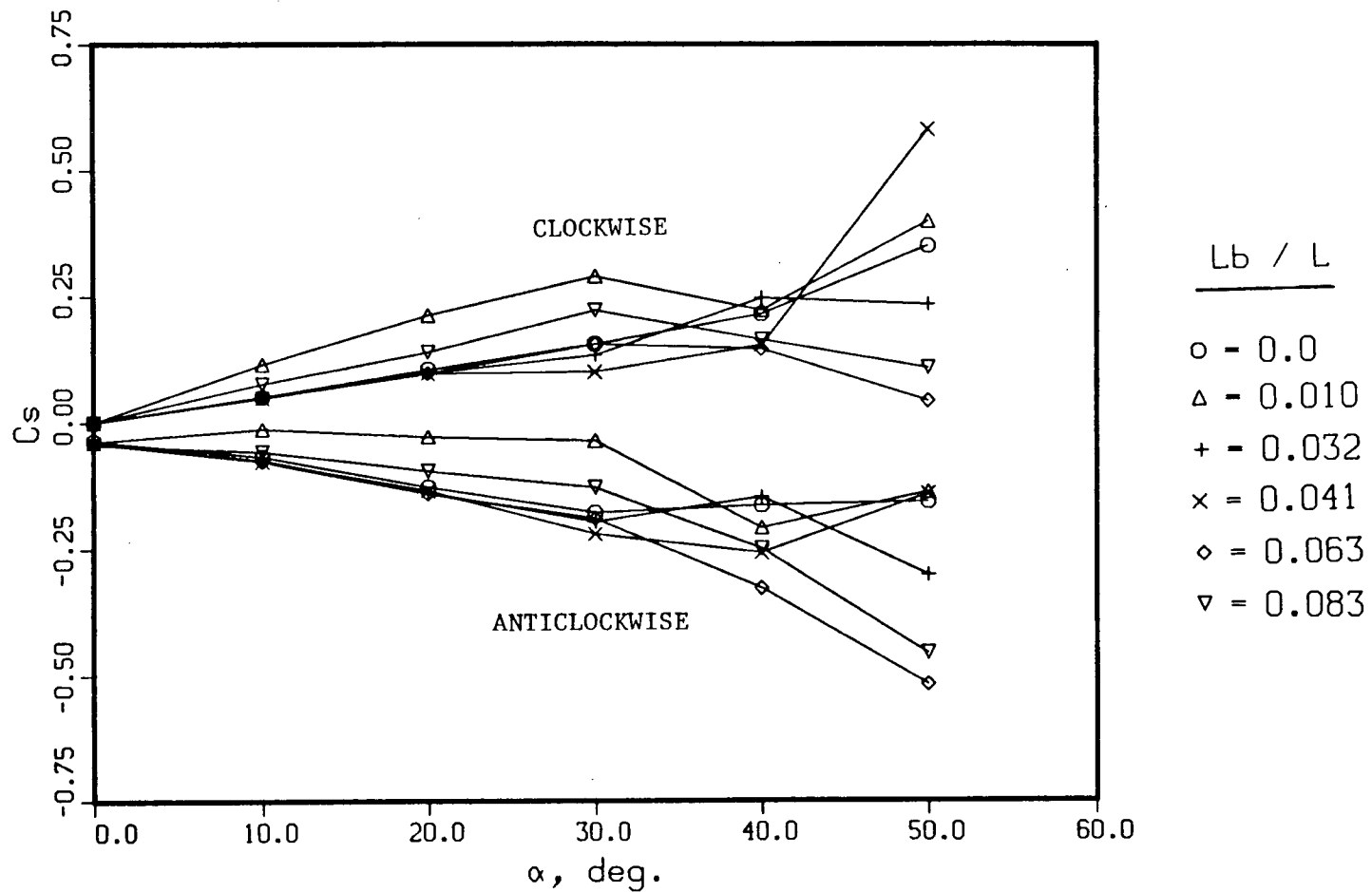


Figure 3-17 Side force variation as affected by pitch angle and nose-boom length at tip spin rate of 2000 rpm .

viewed by the pilot). The opposite is true for the anticlockwise spin. This is in agreement with the results of Ericsson and Reding [15].

- ii) The tip rotation can lead to a significant reduction in the side force. Figure 3-18 demonstrates effectiveness of various nose-booms in reducing the side force at 2000 rpm.

These results show that reduction in the range of 50% to 75% of the nominal value can be obtained by spinning the tip with a nose-boom. The maximum side force reduction with a 0.318 nose-boom tip spinning at 2000 rpm, was around 25% (of the nominal value). Note, the same boom length in the nonspinning tests actually increased the side force from the nominal value. It is interesting to note that the spinning standard tip was quite effective with the side force reduced by 71%.

The second set of tests involved spinning a 1.27 cm nose-boom over a range of speed. The side force variation with the pitch and the spin rate are shown in Figure 3-19. Again the sense of rotation has determined the side force direction. With the present motor it was not possible to obtain a stable spin rate below 100 rpm.

Figures 3-20 shows the maximum side force variation with spin rate for a 1.27 cm nose-boom. Note, a clear minimum in the side force at 200 rpm. In fact, any spin seems to reduce the side force with 200 rpm yielding 25% of the nominal value and 46% of the zero spin case, for the same tip. Investigations by other researchers [12, 15] suggests that the maximum reduction in the side force occurs at spin rates in the range of 100-400 rpm.

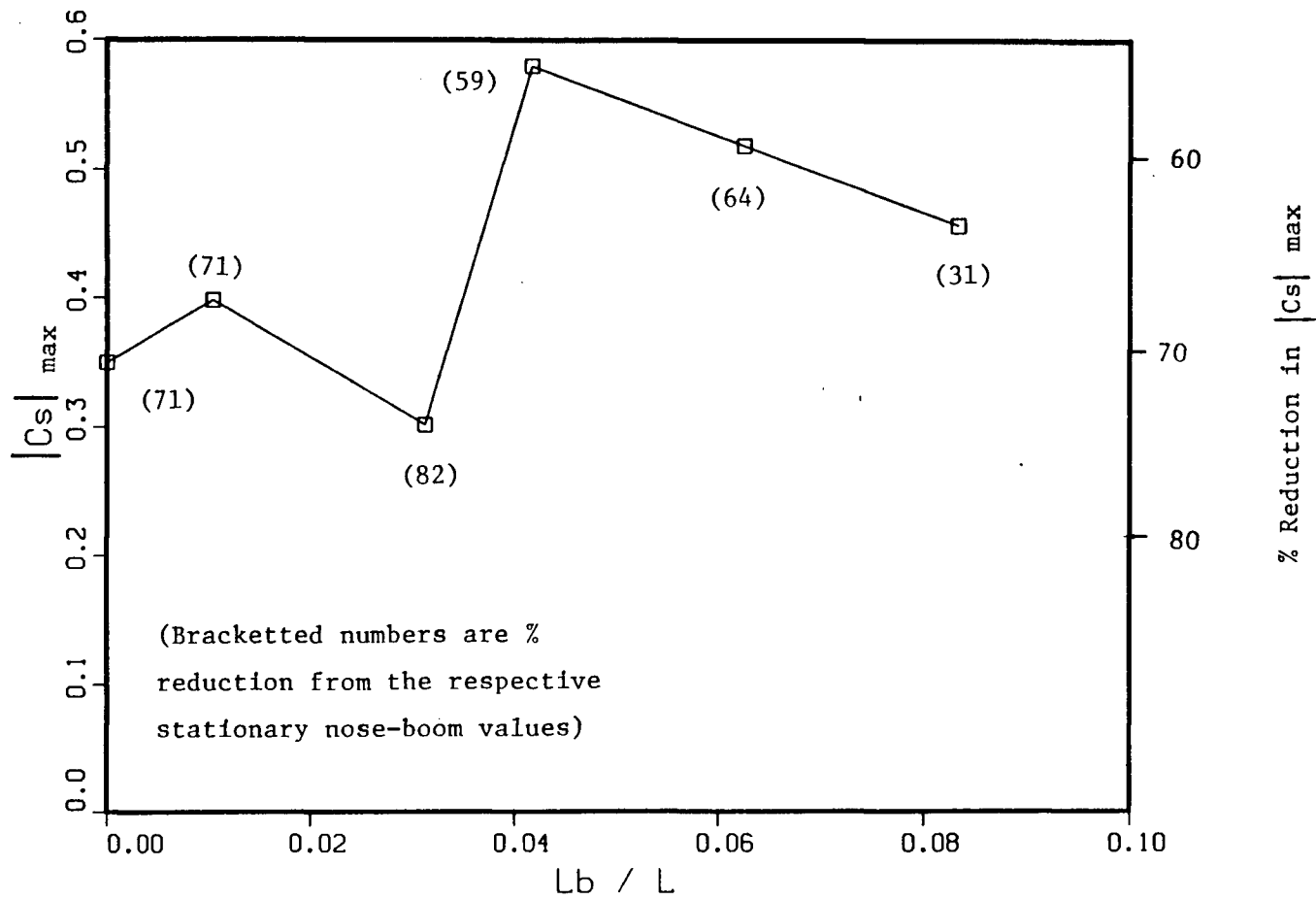


Figure 3-18 Effect of the nose-boom length on the side force coefficient at 2000 rpm.

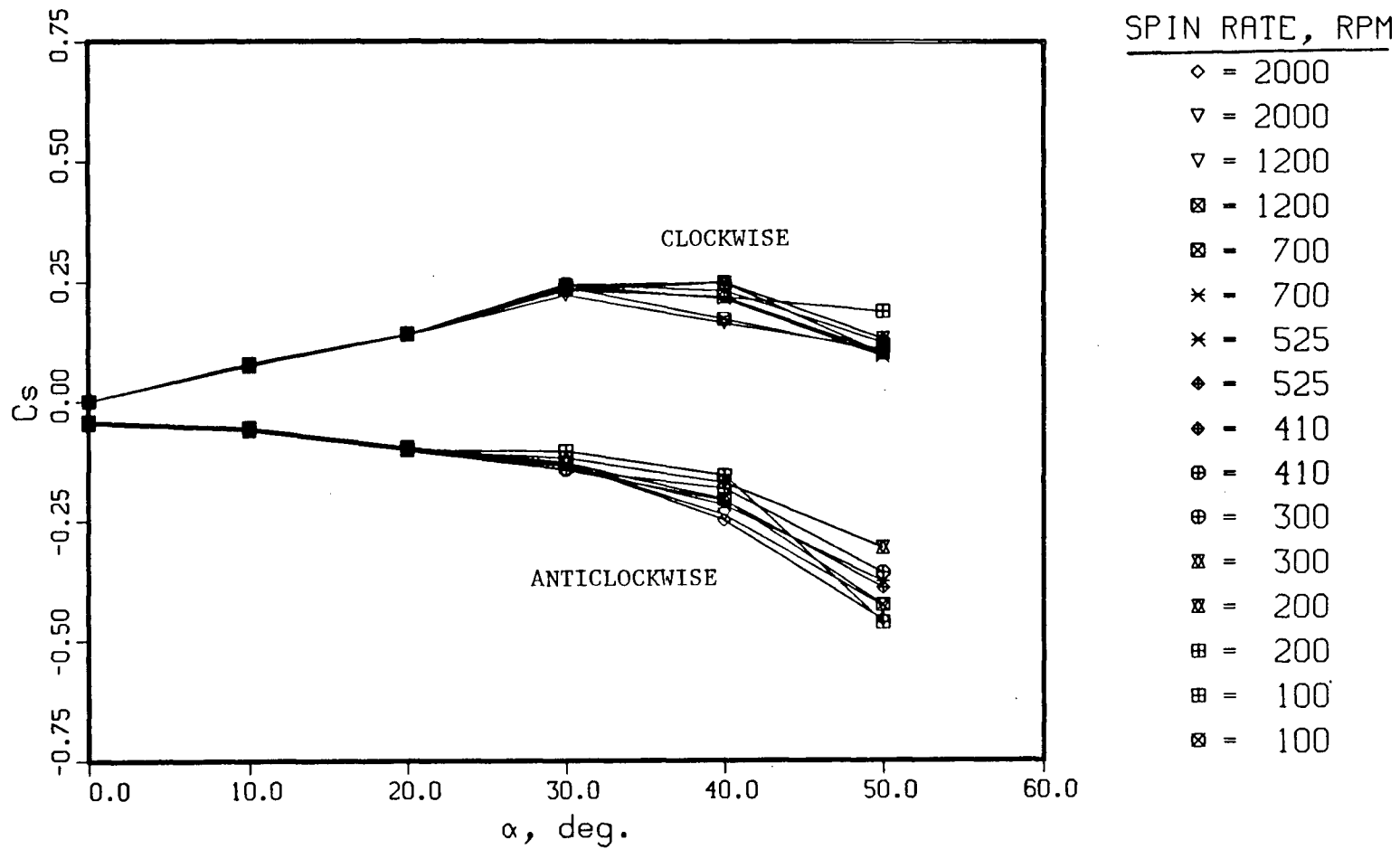


Figure 3-19 Side force variation as affected by pitch angle and spin rate for a 1.27 cm nose-boom.

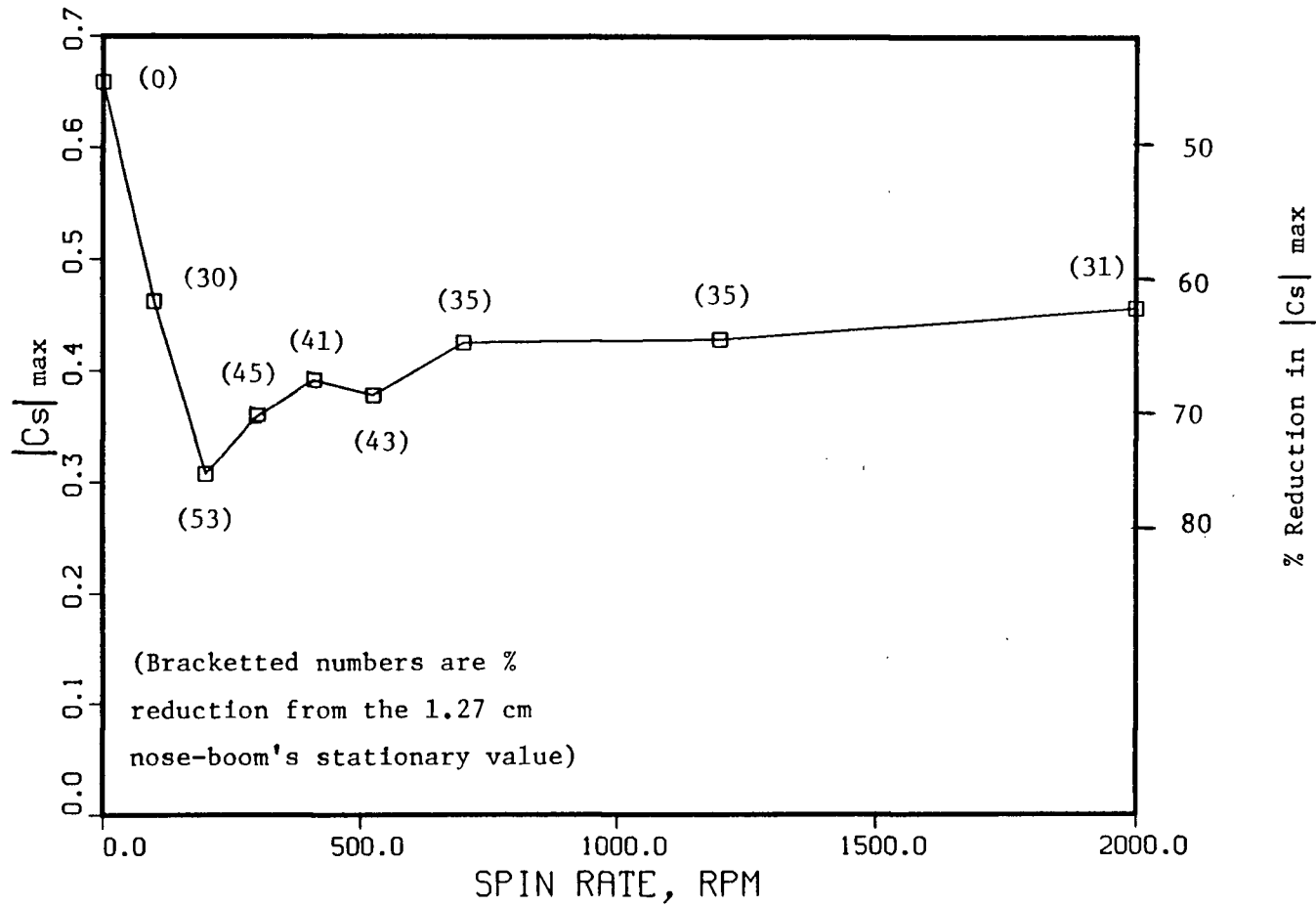


Figure 3-20 Effect of spin rate on the side force coefficient for a 1.27 cm nose-boom.

Results for the normal force coefficient as affected by the boom length and spin rate are presented in Figure 3-21. It is apparent that  $C_n$  is virtually unaffected by these parameters.

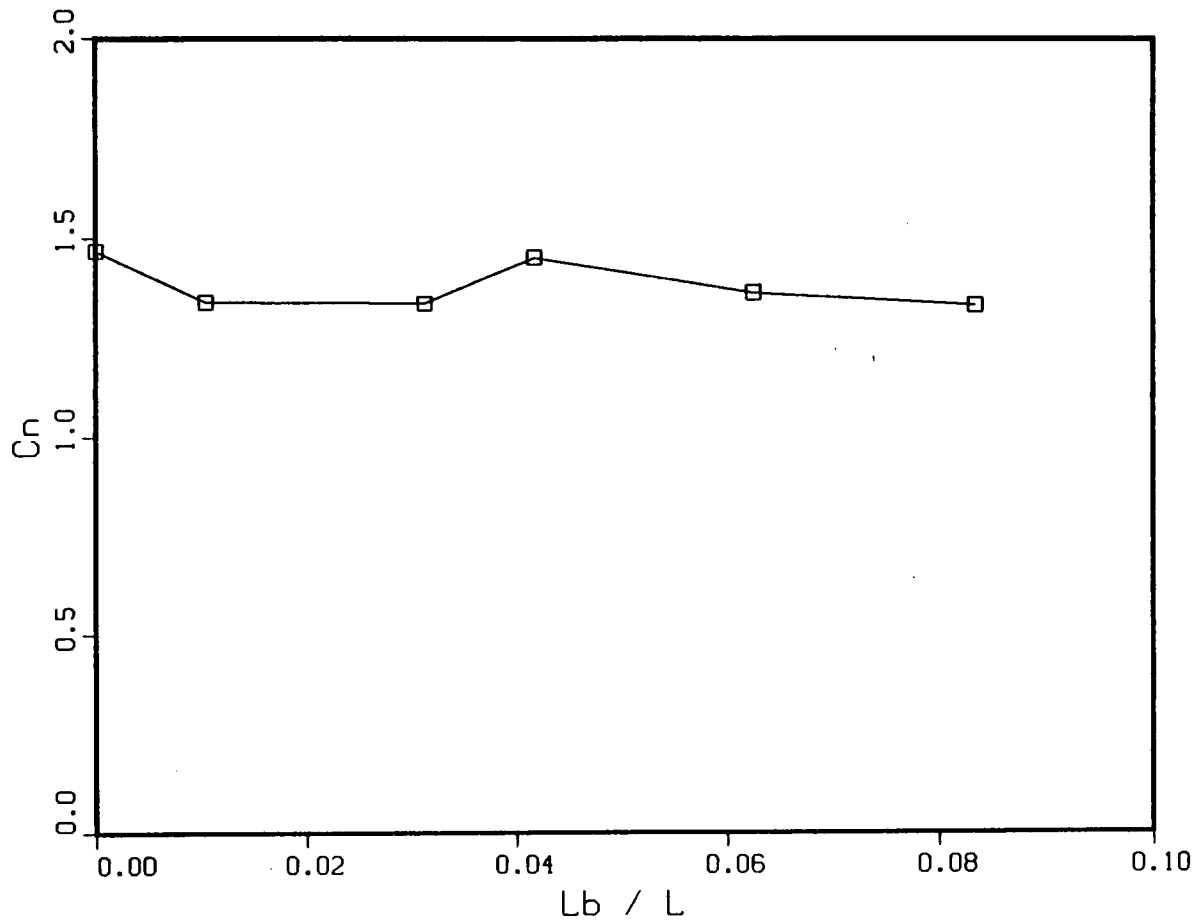


Figure 3-21 The normal force coefficient as affected by:  
a) the nose-boom length at a spin rate of 2000 rpm.

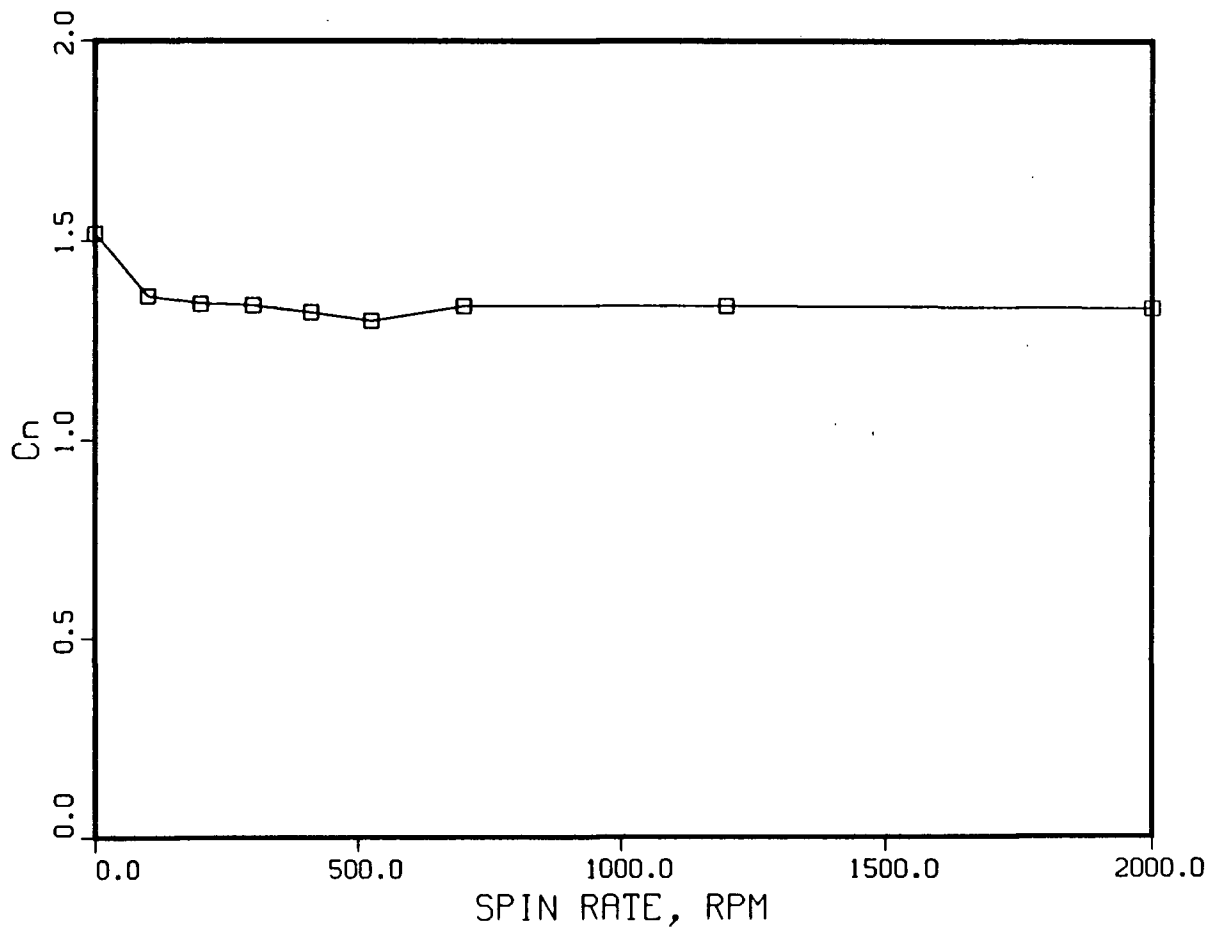


Figure 3-21 The normal force coefficient as affected by:  
b) the spin rate for a 1.27 cm nose-boom.

## 4 CONCLUDING REMARKS

The subject of vortex dominated forebody flows has proven to be far more complex than the first impressions would indicate. As often happens in investigations of aerodynamic phenomena, many uncontrollable parameters appear which not only complicate, but sometimes invalidate the test results. The present study proved to be an education, not only in the subject matter, but in procedures and problems of an involved aerodynamic testing scheme.

### 4.1 Conclusions

The carefully planned experiments with repeatable results provides, for the first time, reliable information concerning the effectiveness of several tip geometries and their rotation on the side force reduction. The tests with a 28° cone-cylinder model, provided with the standard tip, nose-booms without and with porous apex, delta strakes and tip rotation, have given fundamental information leading to a better appreciation of the complex flow. Based on the results following general conclusions can be made:

#### Standard Tip

- i) A complete and authoritative study of side force characteristics at high angles of attack can not be complete without a comprehensive study of effects of the roll angle. Tests must be repeated at as many roll orientations as possible to ensure that the worst configuration is covered.
- ii) Regardless of the hypotheses concerning the side force onset, it is undeniably true that microasymmetry of either

the tip surface or the free stream turbulence is sufficient to trigger asymmetric vortex development. The side force direction switching with roll positions, suggests surface roughness to be an important parameter in initiating an asymmetric flow pattern and the attendant side force.

- iii) The effect of roll orientation can be assessed by either rolling the entire body or the tip alone. This supports the hypothesis that surface asymmetries responsible for triggering major flow asymmetries are confined to the tip region.
- iv) Plots of pressure over the cone surface at high angles of attack show it to be quite low on one half of the leeward side. Based on the literature survey and flow visualization studies by other researchers, the low pressure area is attributed to the presence of a vortex line close to the cone surface. The other half of the leeward side of the cone has a nearly uniform pressure indicating a fully separated flow.
- v) The onset of the significant side force occurs at a pitch angle approximately equal to the cone angle. The maximum side force is of the same order of magnitude as the normal force.
- vi) The normal force is relatively unaffected by the roll orientation.

### Nose-Boom

- i) As in the case of the standard tip, the roll orientation continues to affect the side force, even in the presence of a nose-boom.
- ii) By properly choosing the size of a nose-boom, the side force can be reduced by as much as 50%. However, it appears that too short a nose boom is worse than none at all as a 34% increase in the side force was recorded with a 0.32 cm nose-boom ( $L_b/L = 3.1\%$ ). In fact, the nose-booms shorter than 7% of the cone length increased the maximum side force while the opposite was true for the nose-booms with  $L_b/L > 0.07$ .
- iii) Tests with the nose-booms of lengths less than 7% of the cone length exhibited a greater instability of the flow field. Large changes in the side force magnitude and direction with roll orientations were frequent with shorter booms. This agrees with the trend observed by several investigators in their studies with slender cones.
- iv) The normal force is relatively insensitive to both the nose-boom length and roll orientation.

### Porous Tip with Nose-Boom

- i) A side force reduction of nearly 50% is possible with the addition of a porous tip having a 3.18 cm nose-boom.

### Delta Strake

- i) A side force reduction by at least 88%, and possibly greater, is achievable with an appropriate delta strake. The largest strake used in the test program (21% of the cone length)

exhibited the best side force alleviation. All strakes, irrespective of their lengths, except the shortest (2.1% of the cone length), reduced the side force. The model with the shortest strake behaved almost like the standard tip configuration.

- ii) An orientation of the strake perpendicular to the pitch plane is preferable to that parallel to the pitch plane. A slightly lower side force coefficient results from this more conventional configuration.
- iii) A small roll orientation of the delta strake, as encountered in a noncoordinated flight, leads to a slightly higher side force but still far less than 50% of that encountered with the standard tip.
- iv) Yaw tests with the delta strakes, at  $\beta = \pm 10^\circ$ , indicate that the largest tip promotes a weak but positive directional stability. The stability decreases and the system becomes strongly unstable as the delta strake is reduced in size. The strakes larger than 12% of the cone length appeared to promote directional stability. Incidentally, the same trend was observed for the standard tip model.
- v) A slight decrease in the normal force was observed with the addition of a delta strake. The normal force decreases with an increase in the strake length. For all practical purposes, this negligible reduction in lift is of little consequence compared to the associated large reductions in the side force.

### Spinning Tips

- i) Spin direction determines the direction of the side force. For the test Reynolds number of  $1.1 \times 10^5$ , there is no Magnus lift reversal and the side force is always to the left for clockwise spin and to the right for anticlockwise rotation (as viewed by the pilot).
- ii) Reductions in the side force of up to 75% were possible with spinning tips. Tests with various sizes of the nose-booms spinning at 2000 rpm showed that a smaller boom length is more effective in alleviating the side force. A seventy-five percent reduction in the side force was achieved at 2000 rpm with a 0.32 cm nose-boom.
- iii) Spinning of the nose-tip does not increase the side force.
- iv) A clear minimum side force coefficient (75% reduction) was observed at 200 rpm for the 1.27 cm nose-boom ( $L_b/L = 0.318$ ).
- v) A complex interdependence of the spin rate, tunnel test speed, angle of attack and nose-boom length is evident. A separate more elaborate and carefully planned test-program is necessary to fully appreciate these interactions.

### 4.2 Recommendations

As in any study aimed at understanding a phenomenon at the fundamental level, more new questions arise as one has better appreciation of the process. This experimental program trying to understand the side force phenomenon is no exception. Most of the following recommendations involve extension of the present test-program.

Several of the side force alleviation devices studied here (spinning and porous tips) are of considerable fundamental interest in terms of the associated fluid mechanics and hence merit further investigation on that basis alone. Others (nose-booms and delta strakes), in addition, have considerable scope for practical applications. Depending upon the individual's interest, one or the other group may receive special attention. On the other hand, one may prefer to narrow the wide range of the research topics. Industrial, manufacturing and operational requirements may be polled in order to distinguish feasible side force alleviation devices from those which have little promise in terms of practical application. To this end agencies such as NASA, aircraft and missile manufacturers, pilots and maintenance engineers should also be consulted to evolve a rational plan of further study. Even in absence such coordinated consultation the following recommendations seem appropriate:

- i) Twelve pressure taps per ring is a minimum to adequately describe the pressure distribution. The addition of more pressure taps at certain stations should be seriously considered.
- ii) The model support, although much improved from its previous state [13], could stand further modification. Model vibrations limited the tests to the wind speed (22.7 m/s) and the maximum angle of attack of  $50^\circ$ .
- iii) The use of a reliable and calibrated force balance table is recommended as a check on the pressure integration procedure. The Department of Mechanical Engineering has

just acquired such a system which, unfortunately, was not operational at the time of the present program.

- iv) The use of more complete instrumentation is recommended to better understand the flow field structure around the model. The use of LDV, hot wires and flow visualization, although time consuming would greatly improve the understanding of this flow phenomenon.
- v) The application of various lengths of nose-boom to an aircraft model would prove an interesting and useful substantiation of this work. It is recommended that an F-16 or F-18 aircraft forebody be made or acquired for this purpose as they do not presently incorporate a nose-boom.
- vi) It is recommended that further study of the delta strake tip effectiveness be carried out. This was found to be the best geometry for side force alleviation and as yet has not been optimized. Different lengths, aspect ratios and shapes could be tested to arrive at the optimum geometry. The application of this device to a model of an aircraft nose is also recommended for substantiation of the results.
- vii) Further study of the porous tip concept as a side force alleviation device is recommended. Parameters such as porous length, porosity, and its use with other devices require further examination. A fuel filter made of porous bronze was purchased but proved to be of the wrong shape and size to incorporate into the existing model. Perhaps a new model to match the tip may be constructed to assess its effectiveness.

- viii) The porous tip used in the test program was hollow and connected to the hollow cone model. Pressure was communicated not only circumferentially but also to the wake of the body through the center of the model. It is recommended that the effect of the base pressure on the side force alleviation characteristics be examined by isolating the porous tip cavity from the rest of the model.
- ix) As the side force reduction through tip rotation is an interesting phenomenon, it merits further study. The optimization of spin rate and nose-boom length has not been achieved in the present study. It is recommended that these results be nondimensionalized with respect to the wind speed.
- x) Finally, a statement should be made on an analytical/numerical investigation. Earlier, during the literature review, computer modeling of the complex flow showed little promise. However, recently several authors have developed computer codes, and compared the results of the numerical models with the experimental data, which are encouraging.
- xi) It is suggested that the approaches presented by Newsome and Adams [25], and Fiddes [30] should be explored further, particularly with respect to the various tip geometries and tip rotation. If successful, this would facilitate the design process significantly.

## BIBLIOGRAPHY

- [1] Ericsson L.E., and Reding J.P., "Vortex Induced Asymmetric Loads in 2-D and 3-D Flows", AIAA 18th Aerospace Sciences Meeting, January 14-16, 1980, Pasadena, Calif., Paper No. AIAA-80-0181.
- [2] Allen, H.J., and Perkins, E.W., "Characteristics of Flow Over Inclined Bodies of Revolution", NACA RM A50L07, 1951.
- [3] Thomson, K.D., and Morrison, D.F., "The Spacing, Position and Strength of Vortices in the Wake of Slender Cylindrical Bodies at Large Incidence", Journal of Fluid Mechanics, Vol. 40, Pt. 4, 1971, pp. 751-783.
- [4] Lamont, P.J., and Hunt, B.L., "Pressure and Force Distributions on a Sharp-Nosed Circular Cylinder at Large Angles of Inclination to a Uniform Subsonic Stream", Journal of Fluid Mechanics, Vol. 76, Pt. 3, 1976, pp. 519-559.
- [5] Rao, D.M., "Side-Force Alleviation on Slender, Pointed Forebodies at High Angles of Attack", AIAA Atmospheric Flight Mechanics Conference, August 7-9, 1978, Palo Alto, California, Paper No. AIAA-78-1339.
- [6] Ericsson L.E., and Reding J.P., "Alleviation of Vortex-Induced Asymmetric Loads", Journal of Spacecraft and Rockets. Vol. 17, Nov.-Dec. 1980, pp. 546-553.
- [7] Reding, J.P., and Ericsson, L.E., "Maximum Vortex-Induce Side Force Revisited", AIAA 21st Aerospace Sciences Meeting, January 10-13, 1983, Reno, Nev., Paper No. AIAA-83-0458.

- [8] Peake, D.J., Owen, F.K., and Johnson, D.A., "Control of Forebody Vortex Orientation to Alleviate Side Forces", AIAA 18th Aerospace Sciences Meeting, Jan., 1980, Pasadena, Calif., Paper No. AIAA-80-0183.
- [9] Skow, A.M., Moore, W.A., and Lorincz, D.J., "Control of Forebody Vortex Orientation to Enhance Departure Recovery of Fighter Aircraft", Journal of Aircraft and Rockets, Vol. 19, Oct. 1982, pp. 812-819.
- [10] Erickson, G.E., and Lorincz, D.J., "Water Tunnel and Wind Tunnel Studies of Asymmetric Load Alleviation on a Fighter Aircraft at High Angles of Attack", AIAA 7th Atmospheric Flight Mechanics Conference, Aug., 1980, Danvers, Mass., Paper No. AIAA-80-1618.
- [11] Viswanath, P.R., and Narayan, K.Y., "Side Force Characteristics of a 20° Cone at High Angles of Attack", National Aeronautical Laboratory, Bangalore, India, Technical Memorandum AE 8503, May 1985.
- [12] Modi, V.J., Ries, T., Kwan, A., and Leung, E., "Aerodynamics of Pointed Forebodies at High Angles of Attack", Journal of Aircraft and Rockets, Vol. 21, No. 6, June 1984, pp. 428-432.
- [13] Bishop, W.R., Tarnai, K.V., and Thornthwaite, S.C., "Aerodynamics of Pointed Forebodies at High Angles of Attack", MECH 472 Project Report, Department of Mechanical Engineering, The University of British Columbia, March 1987.
- [14] Oberkampf, W.L., and Bartel, T.J., "Symmetric Body Vortex Wake Characteristics in Supersonic Flow", AIAA Journal, Vol. 18, Nov. 1980, pp. 1289-1297.

- [15] Ericsson L.E., and Reding J.P., "Dynamics of Forebody Flow Separation and Associated Vortices", AIAA Atmospheric Flight Mechanics Conference, August, 1983, Gatlinburg, Tennessee, Paper No. AIAA-83-2118.
- [16] Oberkampf, W.L., Owen, F.K., and Shivananda, T.P., "Experimental Investigation of the Asymmetric Body Vortex Wake", AIAA 18th Aerospace Sciences Meeting, Jan., 1980, Pasadena, Calif., Paper No. AIAA-80-0174.
- [17] Yanta, W.J., and Wardlaw Jr., A.B., "Flow Field About and Force On Slender Bodies at High Angles of Attack", AIAA Journal, Vol. 19, March 1981, pp. 296-302.
- [18] Almosnino, D., and Rom, J., "Lateral Forces on a Slender Body and Their Alleviation at High Incidence", Journal of Spacecraft and Rockets, Vol. 18, Sept.-Oct. 1981, pp. 393-400.
- [19] Peake, D.J., Fisher, D.F., and McRae, D.S., "Flight, Wind Tunnel and Numerical Experiments with a Slender Cone of Incidence", AIAA Journal, Vol. 20, Oct. 1982, pp. 1338-1345.
- [20] Lamont, P.J., "Pressures Around an Inclined Ogive Cylinder with Laminar, Transitional, or Turbulent Separation", AIAA Journal, Vol. 20, Nov. 1982, pp. 1492-1499.
- [21] Keener, E.R., Chapman, G.T., Cohen, L., and Taleghani, J., "Side Forces on a Tangent-Ogive Forebody with a Fineness Ratio of 3.5 at High Angles of Attach and Mach Numbers from 0.1 to 0.7", NASA TM X-3437, Feb. 1977.
- [22] Woolard, H.W., "Similarity Relation for Vortex-Asymmetry Onset on Slender Pointed Forebodies", AIAA Journal, Vol. 20, April 1982, pp. 559-561.

- [23] Almosnino, D., and Rom, J., "Calculation of Symmetric vortex Separation Affecting Subsonic Bodies of High Incidence", AIAA Journal, Vol. 21, March 1983, pp. 398-406.
- [24] Almosnino, D., "High Angle of Attack Calculations of the Subsonic Vortex Flow on Slender Bodies", AIAA 21st Aerospace Sciences Meeting, Jan. 10-13, 1983, Reno, Nev., Paper No. AIAA-83-0035.
- [25] Newsome, R.W., and Adams, M.S., "Vortical Flow over an Elliptical-Body Missile at High Angles of Attack", Journal of Spacecraft and Rockets, Vol. 25, No. 1, Jan.-Feb. 1988, pp. 24-30.
- [26] Chan, Y.Y., "Side Force Computations for Slender Bodies by a Far Field Approach", Journal of Spacecraft and Rockets, Vol. 25, No. 1, Jan.-Feb. 1988, pp. 9-18.
- [27] Seginer, A., and Ringel, M., "Magnus Effects at High Angles of Attack and Critical Reynolds Numbers", AIAA Atmospheric Flight Mechanics Conference, August 15-17, 1983, Gatlinburg, Tennessee, Paper No. AIAA-83-2145.
- [28] Ericsson, L.E., "Flat Spin of Bodies with Circular Cross-Section", AIAA Atmospheric Flight Mechanics Conference, August 15-17, 1983, Gatlinburg, Tennessee, Paper No. AIAA-83-2147.
- [29] Ericsson, L.E., "Flat Spin of Axisymmetric Bodies in the Critical Reynolds Number Range", Journal of Spacecraft and Rockets, Vol. 24, No. 6, Nov.-Dec. 1987, pp. 532-538.
- [30] Fiddes, S.P., "Separated Flow About Cones at Incidence-Theory and Experiment", Studies of Vortex Dominated Flows, Editors: M.Y. Hussaini and M.D. Salas, Springer-Verlag, New York, 1987, pp. 285-310.

- [31] Marconi, F., "On the Prediction of Highly Vortical Flows Using an Euler Equation Model", Studies of Vortex Dominated Flows, Editors: M.Y. Hussaini and M.D. Salas, Springer-Verlag, New York, 1987, pp. 311-364.

## APPENDIX I: INTEGRATION OF PRESSURE DATA

As pointed out earlier, the cone model was provided with 24 to 40 pressure taps depending upon the nose tip used. The cone surface was divided into a number of segments, each surrounding a pressure tap, where the pressure was assumed to be constant. Thus, the force contribution from each segment of the cone surface is the pressure measured at the tap times the area of that segment. The pressure does vary considerably around the cone especially in the circumferential direction, hence the use of this coarse integration procedure does introduce a degree of error of approximately 10%.

Each pressure tap is surrounded by a trapezoidal shaped area segment. The unequal edges are described by a regular polygon of  $n$  sides inscribed in a circle (Figure I-1).

The perimeter ( $C$ ) of the polygon at a reference location  $i$  is

$$C_i = 2nR_i \cdot \sin(\pi/n), \quad \text{hence each side } (S_i) \text{ is given by,}$$

$$S_i = 2R_i \cdot \sin(\pi/n), \quad \text{where the radius } (R_i) \text{ is}$$

$$R_i = L_i \cdot \tan(\delta) \quad \text{and } L_i \text{ is the cone length at station } i.$$

The area ( $A_i$ ) of each trapezoid is

$$A_i = \frac{S_i + S_{(i+n)}}{2} \cdot H_i, \quad \text{where the height of the trapezoid } H_i \text{ is:}$$

$$H_i = \frac{L_i - L_{(i+n)}}{\cos(\delta)}. \quad \text{Thus:}$$

$$A_i = \frac{(L_i^2 - L_{(i+n)}^2) \tan(\delta) \sin(\pi/n)}{\cos(\delta)}$$

The resultant pressure forces exerted upon the cone can now be resolved into normal and side force components as follows:

$$F_N = \text{NORMAL FORCE} = \sum P_i \cdot A_i \cdot \sin \theta_i \cdot \cos(\delta);$$

$$F_s = \text{SIDE FORCE} = \sum P_i \cdot A_i \cdot \cos \theta_i \cdot \cos(\delta); \text{ where } \theta_i \text{ is the circumferential angular position of each pressure tap.}$$

Expressing forces in terms of coefficients:

$$C_N = \frac{\sum C_{p_i} \cdot A_i \cdot \sin \theta_i \cdot \cos(\delta)}{A_B};$$

$$C_s = \frac{\sum C_{p_i} \cdot A_i \cdot \cos \theta_i \cdot \cos(\delta)}{A_B};$$

where  $A_B$  is the cone base area  $\pi D^2/4$ .

As drag and axial forces were not measured, the use of normal force instead of lift force is more logical and conventional in this type of investigation.

The FORTRAN program used to integrate the pressure data is attached.

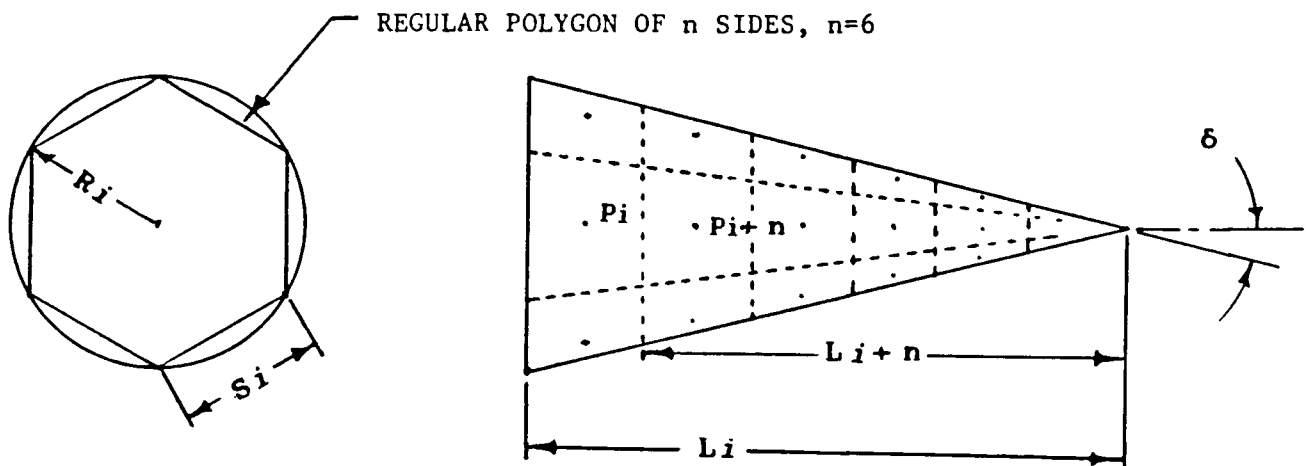


Figure I-1 Division of the cone surface into area segments.

```

C PROGRAM TO RESOLVE FORCES ON A CONE
C INTO LIFT DRAG AND SIDE FORCE
  REAL A(40),CP(41),L(40),T(40),LIFT,TT(12),CPP(12)
  INTEGER ALPHA1,ALPHA2,NOSE,ROLL
  CHARACTER TEST*30
C A IS THE ARE SURROUNDING EACH PRESSURE TAP
C CP IS THE COEFFICIENT OF PRESSURE FOR EACH TAP
C L IS THE LENGTH OF EACH AREA SEGMENT MEASURED
C                                     FROM THE TIP
C T IS THE ORIENTATION IN ROLL OF EACH TAP
C CA IS THE CONE HALF ANGLE
C ALPHA1 IS THE FIRST ANGLE OF ATTACK FOR EACH TEST
C ALPHA2 IS THE LAST ANGLE OF ATTACK FOR EACH TEST
C NOSE IS THE NOSE ROLL POSITION
C ROLL IS THE BODY ROLL POSITION
C TEST IS THE TITLE OF EACH EXPERIMENT
C
C
C FIRST FOR THE AREAS
  PI=3.1415926
  CA=ATAN(.25)
  L(1)=6.0
  L(7)=5.0
  L(13)=4.125
  L(19)=3.25
  L(25)=2.25
  L(37)=1.25
  DO 1 N=1,5
    L(1+N)=L(1)
    L(7+N)=L(7)
    L(13+N)=L(13)
    L(19+N)=L(19)
  1 L(41-N)=L(37)
  DO 8 N=1,11
    L(25+N)=L(25)
  DO 2 N=1,24
  2 A(N)=(L(N)**2-L(N+6)**2)*TAN(CA)/COS(CA)/2.
  DO 3 N=25,36
  3 A(N)=(L(N)**2-L(37)**2)*TAN(CA)*SIN(PI/12.)/COS(CA)
  DO 12 N=37,40
  12 A(N)=L(N)**2*TAN(CA)/COS(CA)*SIN(PI/4.)
C
C DO LOOP FOR VARIOUS TESTS
C
  DO 7 J=1,24
C
C DO LOOP FOR VARIOUS ANGLES OF ATTACK
C INPUT ROLL ANGLE, ANGLE OF ATTACK, NOSE POSITION
C
  READ(5,70) TEST
  70 FORMAT(A30)
  WRITE(7,70)TEST
  READ*,ROLL,ALPHA1,ALPHA2
  WRITE(7,25)ROLL,ALPHA1,ALPHA2
  25 FORMAT(3(I5))
C
C CALCULATE TAP ROLL POSITION
C
  T(1)=(3.0+ROLL)*PI/6.0
  T(2)=(5.0+ROLL)*PI/6.0
  T(3)=(7.0+ROLL)*PI/6.0
  T(4)=(9.0+ROLL)*PI/6.0
  T(5)=(11.0+ROLL)*PI/6.0
  T(6)=(1.0+ROLL)*PI/6.0
  DO 4 N=1,3
    T(6*N+1)=T(1)
    T(6*N+2)=T(2)
    T(6*N+3)=T(3)
    T(6*N+4)=T(4)
    T(6*N+5)=T(5)
  4 T(6*N+6)=T(6)

```

```

      T(25)=T(1)-.3578
      DO 9 N=1,11
    9  T(25+N)=T(24+N)+PI/6.
      T(37)=T(25)
      DO 11 N=1,3
    11 T(37+N)=T(36+N)+PI/2.
      DO 21 N=1,40
      PI2=2.*PI
    21 IF(T(N).GE.PI2) T(N)=T(N)-PI2
C
C INPUT PRESSURE MEASUREMENTS
C
      DO 7 K=ALPHA1,ALPHA2,10
      READ(5,20)CP
    20 FORMAT(12(F10.4))
      Q=CP(41)
      DO 5 N=1,41
    5  CP(N)=CP(N)/Q
C SORTING OF ANGLES AND PRESSURES
      LF=25
      DO 22 N=26,36
    22 IF(T(LF).GT.T(N)) LF=N
      DO 23 N=1,12
      LFF=LF+N-1
      IF(LFF.GT.36) THEN
        KK=LF+N-13
      ELSE
        KK=LF+N-1
      ENDIF
    23 CPP(N)=CP(KK)
      WRITE(7,35)TT
    35 FORMAT(12(F10.4))
      WRITE(7,35)CPP
C
C INTEGRATE FORCES
C
      LIFT=0.0
      SIDE=0.0
      DO 6 N=1,40
    6  SIDE=SIDE+A(N)*CP(N)*COS(CA)*SIN(T(N))
      CL=LIFT/(2.25*PI)
      CS=SIDE/(2.25*PI)
C
C NOW FOR SOME RESULTS
C
      WRITE(6,60) TEST
    60 FORMAT(2X,A30)
C      WRITE(6,40) ROLL,K,CL,CS
    40 FORMAT(5X,'FOR ROLL POSITION ',I3,' AND FOR ANGLE ',
      2' OF ATTACK ',I3,
      3' CL AND CS ARE ',2(F10.4))
      WRITE(7,45)CL,CS
    45 FORMAT(2(F10.4))
C      WRITE(6,50)
    50 FORMAT(' PRESSURE COEFFICIENTS FOR EACH TAP')
C      WRITE(6,30) CP
    30 FORMAT(6(F10.4))
C      7 CONTINUE
      STOP
      END

```